The Astrophysical Journal, 759:98 (29pp), 2012 November 10 doi:10.1088/0004-637X/759/2/98

BREAKS IN THIN AND THICK DISKS OF EDGE-ON GALAXIES IMAGED IN THE *SPITZER* SURVEY OF STELLAR STRUCTURE IN GALAXIES (S^{4}G)

Sébastien Comerón[1,2], Bruce G. Elmegreen[3], Heikki Salo[1], Eija Laurikainen[1,4], E. Athanassoula[5], Albert Bosma[5], Johan H. Knapen[6,7], Dimitri A. Gadotti[8], Kartik Sheth[9], Joannah L. Hinz[10], Michael W. Regan[11], Armando Gil de Paz[12], Juan Carlos Muñoz-Mateos[9], Karín Menéndez-Delmestre[13], Mark Seibert[14], Taehyun Kim[9], Trisha Mizusawa[15], Jarkko Laine[1], Luis C. Ho[14], and Benne Holwerda[16]

[1] Astronomy Division, Department of Physics, University of Oulu, P.O. Box 3000, FI–90014, Finland
[2] Korea Astronomy and Space Science Institute, 776 Daedeokdae-ro, Yuseong-gu, Daejeon 305-348, Republic of Korea
[3] IBM T. J. Watson Research Center, 1101 Kitchawan Road, Yorktown Heights, NY 10598, USA
[4] Finnish Centre of Astronomy with ESO (FINCA), University of Turku, Väisäläntie 20, FI–21500 Piikkiö, Finland
[5] Laboratoire d'Astrophysique de Marseille-LAM, Université d'Aix-Marseille & CNRS, UMR7326, 38 rue F. Joliot-Curie, F-13388 Marseille Cedex 13, France
[6] Instituto de Astrofísica de Canarias, E-38200 La Laguna, Spain
[7] Departamento de Astrofísica, Universidad de La Laguna, E-38205 La Laguna, Tenerife, Spain
[8] European Southern Observatory, Casilla 19001, Santiago 19, Chile
[9] National Radio Astronomy Observatory, Charlottesville, VA, USA
[10] Department of Astronomy, University of Arizona, Tucson, AZ, USA
[11] Space Telescope Science Institute, Baltimore, MD, USA
[12] Departamento de Astrofísica, Universidad Complutense de Madrid, Madrid, Spain
[13] Observatorio do Valongo, Universidade Federal de Rio de Janeiro, Ladeira Pedro Antônio, 43, Saúde CEP 20080-090, Rio de Janeiro-RJ-Brazil
[14] The Observatories of the Carnegie Institution for Science, Pasadena, CA, USA
[15] Department of Physics and Space Sciences, Florida Institute of Technology, 150 W. University Boulevard, Melbourne, FL32901
[16] European Space Agency, ESTEC, Keplerlaan 1, 2200-AG, Noordwijk, The Netherlands
Received 2012 April 24; accepted 2012 September 2; published 2012 October 25

ABSTRACT

Breaks in the radial luminosity profiles of galaxies have until now been mostly studied averaged over disks. Here, we study separately breaks in thin and thick disks in 70 edge-on galaxies using imaging from the Spitzer Survey of Stellar Structure in Galaxies. We built luminosity profiles of the thin and thick disks parallel to midplanes and we found that thin disks often truncate (77%). Thick disks truncate less often (31%), but when they do, their break radius is comparable with that in the thin disk. This suggests either two different truncation mechanisms—one of dynamical origin affecting both disks simultaneously and another one only affecting the thin disk—or a single mechanism that creates a truncation in one disk or in both depending on some galaxy property. Thin disks apparently antitruncate in around 40% of galaxies. However, in many cases, these antitruncations are an artifact caused by the superposition of a thin disk and a thick disk, with the latter having a longer scale length. We estimate the real thin disk antitruncation fraction to be less than 15%. We found that the ratio of the thick and thin stellar disk mass is roughly constant ($0.2 < M_T/M_t < 0.7$) for circular velocities $v_c > 120\,\mathrm{km\,s^{-1}}$, but becomes much larger at smaller velocities. We hypothesize that this is due to a combination of a high efficiency of supernova feedback and a slower dynamical evolution in lower-mass galaxies causing stellar thin disks to be younger and less massive than in higher-mass galaxies.

Key words: galaxies: photometry – galaxies: spiral – galaxies: structure

Online-only material: color figures, extended figure

1. INTRODUCTION

Thick disks are defined to be disk-like components with a scale height larger than that of the "canonical" or "classical" disks. They are most easily detected in close to edge-on galaxies in which they appear as a roughly exponential excess of light a few thin disk scale heights above the midplane. They were first detected and described by Tsikoudi (1979) and Burstein (1979). The Milky Way was soon found to also host a thick disk (Gilmore & Reid 1983) made of old (Bensby et al. 2005), metal-poor, and α-enhanced stars (Fuhrmann 1998; Prochaska et al. 2000). Observations now suggest that thick disks in galaxies in the local universe are ubiquitous (Yoachim & Dalcanton 2006; Comerón et al. 2011c).

We recently showed evidence of thick disks being significantly more massive than previously considered with stellar masses ranging from 0.3 to 3.0 times that of the thin disk depending on the galaxy mass and the assumed mass-to-light ratios (Comerón et al. 2011b, hereafter CO11b). This study confirmed that galaxies dominated by the thick disk are usually those with lower masses (Yoachim & Dalcanton 2006). Hosting such a large fraction of the stellar mass makes thick disks likely reservoirs of some of the "local missing baryons." A few galaxies, such as NGC 4013, host an additional extended component which could be interpreted as a second thick disk or a flattened halo (Comerón et al. 2011a).

The properties of those more massive than expected thick disks give some constraints on their origin. Higher mass galaxies could have their thick disks with a low relative mass explained by internal secular heating (see, e.g., Bovy et al. 2012), by the heating caused by the interaction with a satellite galaxy (see, e.g., Qu et al. 2011), by the accretion of stars from satellite galaxies (see, e.g., Abadi et al. 2003), and/or because of the radial migration of stars (see, e.g., Schönrich & Binney 2009;

Loebman et al. 2011), but the very large thick disk mass fraction found in low-mass galaxies indicates an in situ origin during or shortly after the buildup of the galaxy for a large fraction of their thick disk stars.

Two in situ and high-redshift thick disk formation models have been put forward. Elmegreen & Elmegreen (2006) and Bournaud et al. (2009) proposed a scenario where the thick disk forms from the primordial galaxy disks, which contained large clumps of star formation whose scale height was comparable to that of present-day thick disks. Those large clumps would have dissolved into what we know as thick disks. Brook et al. (2007) proposed thick disks to be made of stars in gas-rich protogalactic fragments which merged and of stars created during that merger. In both scenarios, the thin disk would have formed afterward from gas remaining from the initial galaxy formation processes and from new gas accreted through cold flows. These two models predict different properties for the thick disks. If they have been created from the dissolution of giant star-forming clusters, then one would expect them to be genuine disks, with a high rotation speed and a luminosity profile similar to that of thin disks. If thick disks result from the merger of protogalactic fragments, then they would, at least in some cases, host a significant fraction of lagging and/or counterrotating stars.

Our comprehensive detection and modeling of thick+thin disks in edge-on galaxies started in CO11b allow us to study breaks, both truncations and antitruncations, in the radial profile of the thick disks, hitherto impossible. A radical truncation in the radial light profile in edge-on galaxies was first discussed by van der Kruit (1979) and van der Kruit & Searle (1981a, 1981b, 1982). The break phenomenon is widely observed in local galaxies (van der Kruit & Searle 1981b; Barteldrees & Dettmar 1994; Pohlen et al. 2000; de Grijs et al. 2001; Florido et al. 2001; Kregel et al. 2002; Kregel & van der Kruit 2004; Pohlen & Trujillo 2006; Florido et al. 2006a, 2006b) and at high redshift (Pérez 2004; Trujillo & Pohlen 2005). See for reviews of these optical studies van der Kruit (2001) and Pohlen et al. (2004b).

Galaxies have been divided into three types depending on their disk properties: Type I, with an unbroken exponential (Freeman 1970); Type II (truncation), hosting a downbending break; and Type III (antitruncation), hosting a transition to a shallower exponential profile (Pohlen & Trujillo 2006; Erwin et al. 2008), based on averaged radial light profiles. This opens the possibility that some of the observed characteristics may be due to the superposition of the thin and thick disks in these galaxies. Due to the low-surface-brightness nature of the thick disk, this was left mostly unexplored. Pohlen et al. (2004a, 2007) do suggest a weakening of the truncation with height moving from the thin to the thick disk-dominated regime. This has been confirmed by *Hubble Space Telescope* observations over two truncations for all stellar populations (de Jong et al. 2007; Radburn-Smith et al. 2012).

The origin of truncations and antitruncations is under debate. The former are hypothesized to be formed due to star formation thresholds (Kennicutt 1989), the point of maximum angular momentum of the original primordial cloud from which the galaxy has formed (van der Kruit 1987), and/or by bar angular momentum redistribution (Debattista et al. 2006). Laurikainen & Salo (2001) proved that many M 51-like galaxies have an antitruncation caused by the stripping of stars and gas from the disk during the interaction. They numerically showed that these antitruncations could last for several Gyr. Also, a few antitruncations (15%) seem to be caused by the contribution of an extended bulge to the luminosity profile (Maltby et al. 2012).

The main purpose of this paper is to obtain the luminosity profiles of thin and thick disks of nearly edge-on galaxies parallel to their midplane in order to further constrain their origin. We also study truncations and antitruncations in thin and thick disks as separate features by fitting their luminosity profiles with a generalization of the function proposed by Erwin et al. (2008) for the description of disks with breaks.

We used images from the Spitzer Survey of Stellar Structure in Galaxies (S^4G; Sheth et al. 2010), which has imaged more than 2000 galaxies representative of the nearby universe (radial velocity $V_{\rm radio} < 3000\,{\rm km\,s^{-1}}$) in 3.6 μm and 4.5 μm using the Infrared Array Camera (IRAC; Fazio et al. 2004). The S^4G reaches a typical surface brightness of $\mu_{3.6\,\mu{\rm m}}({\rm AB})(1\sigma) \sim 27\,{\rm mag\,arcsec^{-2}}$ with a pixel size of 0.″75 and mostly traces the light of old stars with little dust absorption, which makes it ideal for the study of edge-on galaxies.

This paper is structured as follows. We present the selected sample in Section 2 and we describe the fitting procedure in Section 3. We continue in Section 4 by addressing what would happen if some assumptions made when producing the fits were not applicable to our sample of galaxies. We show and discuss our results in Sections 5 and 6, and we present our conclusions in Section 7.

2. GALAXY SAMPLE

We looked at each of the 2132 galaxies available in the S^4G archive by February 15, 2012 and we manually selected disk galaxies appearing to be edge-on with morphological types $-3 \leqslant T < 8$ (T from HyperLEDA; Paturel et al. 2003). Later type galaxies were rejected because of their generally ill-defined structure. We have assumed that T can be "reasonably reliably" determined for edge-on galaxy as claimed by Buta (2012).

We also rejected galaxies with distorted morphologies, with indications of being not quite edge-on (with visible spiral arms or resonance rings), or disks that are too dim to certainly assess their orientation. When possible, Sloan Digital Sky Survey Data Release 8 (Aihara et al. 2011) imaging was used in order to ensure close to edge-on galaxy orientation by looking at the position of the midplane dust.

The resulting sample has 169 galaxies which includes 29 out of 30 galaxies studied in detail in CO11b. The remaining galaxy, IC 1970, was excluded due to some hint of spiral structure. All those galaxies underwent the image processing and fitting procedure described in Sections 3.2 and 3.3. In Section 3.5, we describe how, after fitting thin+thick+gas disk profiles to galaxy luminosity profiles perpendicular to their midplanes, we applied additional selection criteria aiming to remove faint galaxies, galaxies with extended envelopes, and/or badly fitted galaxies, in order to ensure the data quality and we built up a final sample with 70 galaxies.

3. LUMINOSITY PROFILE FITTING

In order to obtain luminosity profiles of thin and thick disks parallel to galaxy midplanes and to study them, we followed a procedure that is described in detail in the next subsections.

1. We prepared a grid of synthetic luminosity profiles perpendicular to the galaxy midplanes, as done in CO11b. The selected profile was that of a combined thin, thick, and gas disk gravitationally coupled in local isothermal equilibrium for galaxies with $T \geqslant 1$. For earlier-type galaxies, we only considered a thin and a thick disk. (Section 3.1).

2. We extracted the observed luminosity profiles perpendicular to galaxy midplanes using an average of 3.6 and 4.5 μm band S^{4}G images (vertical luminosity profiles; Section 3.2).
3. We fitted the observed luminosity profiles by comparing them with the grid of synthetic models as done in CO11b (Section 3.3).
4. Using the vertical luminosity profile fits, we determined the height, z_s, above which the thick disk dominates the light emission (Section 3.4).
5. By looking at the properties of vertical luminosity profile fits and the resulting z_s, we trimmed the 169 galaxy sample down to 70, in order to ensure the quality of the data. The galaxy rejection criteria aimed to remove galaxies with bad fits, that were extended envelopes, or too faint and thus had noisy luminosity profiles (Section 3.5).
6. Knowing z_s has allowed us to determine the region dominated by the thin and thick disk light; thus, we have been able to prepare luminosity profiles of the thin and thick disks parallel to the galaxy midplanes. We also prepared a profile including light from both disks (horizontal luminosity profiles; Section 3.6).
7. The horizontal luminosity profiles of both the thin and thick disks, as well as those including light from both, were fitted with a generalization of the function used by Erwin et al. (2008) to describe disks with breaks (Section 3.7).

3.1. Synthetic Luminosity Profiles Perpendicular to Galaxy Midplanes

In order to prepare thin and thick disk luminosity profiles parallel to the midplane of a galaxy, it is fundamental to know in which range in heights above the midplane each disk dominates. To do so, we fitted luminosity profiles perpendicular to galaxy midplanes with thin+thick+gas disk functions for galaxies with $T \geqslant 1$. For earlier-type galaxies, we set the gas disk to have a zero density, which is equivalent to assuming a thin+thick disk function. Assuming little or no gas in these galaxies solves one of the fitting biases discussed in Section 4.3.2, namely, that of gas-depleted galaxies with a thick disk mass overestimated due to fitting with a function accounting for gas.

As in CO11b, we assumed that galaxy disks are relaxed structures whose particles behave like those of a fluid in equilibrium. We also assumed that disks are made of three gravitationally coupled baryonic disks—gas disk, thin disk, and thick disk—which feel the effect of something acting like a dark matter halo. Then, we can write following the equation from Narayan & Jog (2002)

$$\frac{d^2\rho_i}{dz^2} = \frac{\rho_i}{\sigma_i^2}(-4\pi \mathrm{G}(\rho_t + \rho_T + \rho_\mathrm{g}) + \frac{dK_\mathrm{DM}}{dz}) + \frac{1}{\rho_i}\left(\frac{d\rho_i}{dz}\right)^2, \quad (1)$$

where t refers to the thin disk, T to the thick disk, and g to the gas disk; the subindex i can be either t, T, or g, ρ stands for the mass density, and σ for the vertical velocity dispersion of the component. dK_DM/dz is the term describing dark matter effects. This is a set of three coupled second-order differential equations which we solved by using the Newmark-β method with $\beta = 0.25$ and $\gamma = 0.5$. β and γ are internal parameters of the algorithm which have been set to make it unconditionally stable (Newmark 1959).

When integrating Equation (1), we assumed that the isothermal hypothesis is true. This hypothesis implies that for a given galactic radius, r, the vertical velocity dispersion is constant with height, z ($\sigma(r, z) = \sigma(r)$). We also assumed that the effect of dark matter is negligible ($dK_\mathrm{DM}/dz = 0$; see justification in CO11b and Section 4). Line-of-sight effects were avoided by assuming that all of the disks have similar scale lengths and that the scale heights remain roughly constant with varying r. This last assumption is based on the fact that S^{4}G disks do not flare significantly within the optical radius and has been widely used in the literature (van der Kruit & Searle 1981a; Yoachim & Dalcanton 2006; CO11b). We also assumed that the face-on gas surface mass density for galaxies with $T \geqslant 1$ is 0.2 times that of the thin disk at all radii. A 20% gas fraction is slightly higher than that found in the Milky Way at solar radius (Banerjee & Jog 2007) and we have shown in CO11b that it yields slightly better fits than when not accounting for gas. It is also a fraction of gas representative of what is found in our galaxy sample according to our gas fraction calculations presented in Section 6.3. We set $\rho_\mathrm{g} = 0$ for galaxies with $T < 1$. Finally, we assumed $\sigma_\mathrm{g} = 1/3\sigma_t$ in rough accordance with Milky Way velocity dispersion measurements (Spitzer 1978; Stark 1984; Clemens 1985; Lewis & Freeman 1989).

Equation (1) provides mass density profiles. For obtaining luminosity profiles, some assumptions about Υ_t and Υ_T, the mass-to-light ratios of the thin and thick disks, were needed. Different Υ_T/Υ_t values can be calculated from different star formation histories for the thin and thick disks. Reasonable star formation histories yield $1.2 < \Upsilon_T/\Upsilon_t < 2.4$ (see in the discussion in Section 3.3 in CO11b). In this paper, we use the most conservative value—that with lower relative thick disk masses—$\Upsilon_T/\Upsilon_t = 1.2$.

When integrating Equation (1), six boundary conditions are needed. Since the maximum density is found in the midplane, we set $d\rho_i/dz|_{z=0} = 0$. The other boundary conditions we used are the mass densities of each disk in the midplane $\rho_i(z = 0)$ (hereafter ρ_{i0}).

We solved Equation (1) for a grid of models with different central density ratios (ρ_{T0}/ρ_{t0}) and different vertical velocity dispersion ratios, σ_T/σ_t. We made integrations for 150 values of ρ_{T0}/ρ_{t0}, equally spaced from 0.015 to 2.25, and for 150 values of $(\sigma_T/\sigma_t)^2$, equally spaced from 1.1 to 16.0. The solutions in this grid were then compared to observed luminosity profiles as described in the following subsections.

3.2. Observed Luminosity Profiles Perpendicular to Galaxy Midplanes

We selected the 3.6 and 4.5 μm band images for the 169 galaxies in our original sample and we subtracted the background from each image. The background was measured by selecting several tens of 5×5 pixel boxes far away from the midplane of the galaxy and bright stars and then by obtaining the median value of the pixels in the box. The selected background value was that of the median of the individual medians found for each box. The angular distance between the boxes in which we measured the background and the midplane of the galaxy for galaxies fitting in the IRAC chip ($D_{25} < 3.'3$; Sheth et al. 2010) is limited by IRAC's field of view ($5.'2 \times 5.'2$) and is typically around $100''$. For the few galaxies which required a mosaic, the sky has been measured in boxes as close to the border of the mosaic as possible in the direction perpendicular to the midplane.

The median distance of the galaxies for which we studied the breaks is 29.8 Mpc (see Section 3.5 for details on the original sample trimming). At that distance, $100''$ correspond to 14.4 kpc, which may cause our estimated sky value to actually be the stellar halo level. Bakos & Trujillo (2012)

found that halos start affecting the luminosity profiles of galaxies at $r' \sim 28$ mag arcsec^{-2}. Because we have not found color indices including IRAC filters for stellar halos in the literature, we have used globular cluster colors as a proxy for halo colors in order to test whether this error in the sky subtraction could affect our analysis. The reddest globular cluster in the sample of Spitler et al. (2008) has $R(\mathrm{AB}) - \mu_{3.6\,\mu\mathrm{m}}(\mathrm{AB}) \sim 0.8$. This globular cluster has $V - R \sim 0.55$ (Spitler et al. 2008) and using the color transformations for Population II stars in Jordi et al. (2006), we can affirm that $r'(\mathrm{AB}) \sim R(\mathrm{AB})$ within 0.1 mag. That implies that the halo would start affecting our luminosity profiles at $\mu_{3.6\,\mu\mathrm{m}}(\mathrm{AB}) \sim 27$ mag arcsec^{-2}. Since our break detection limit is within the range $\mu_{3.6\,\mu\mathrm{m}} = 25$–$26$ mag arcsec^{-2} (see Section 5.4), stellar halos are not likely to affect our analysis of the background for subtraction.

Typical 1σ errors of the background determination of the addition of the 3.6 and 4.5 μm images are around 0.0015 counts, corresponding to a surface brightness level of $\mu = 27.5$ mag arcsec^{-2}. This error bar was measured by finding the standard deviation of different background values obtained using bootstrapping over the local background values in the individual 5×5 pixel boxes. The value of the measured background does not vary significantly when increasing the box size from 5×5 to 9×9 pixels. However, the background error is rarely the limiting factor when fitting the luminosity profiles; the actual main limiting factor is the quality of the mask, as explained at the end of Section 3.3.

Using the average of the sky-subtracted 3.6 and 4.5 μm band images, we produced four luminosity profiles for each galaxy: at each side of the bulge, central cluster, or presumed center along the disk long axis for projected galactocentric distances $0.2r_{25} < |R| < 0.5r_{25}$ and $0.5r_{25} < |R| < 0.8r_{25}$ (top panel in Figure 1). We used r_{25} values from HyperLEDA, except for NGC 4111, for which we preferred the Third Reference Catalog of Bright Galaxies value (RC3; de Vaucouleurs et al. 1991) due to the HyperLEDA value being clearly underestimated. The profiles were prepared by adding the counts above and below the midplane in order to get a unique profile for each bin and averaging for each z over non-masked pixels. We used manually refined masks from the S^{4}G Pipeline 2 (Sheth et al. 2010). The flux was transformed into magnitudes using a zero point $z_p = 20.472$.

We increased the signal to noise at low surface brightness levels by smoothing the luminosity profiles. To do so, we found the height of the first profile data point for which the statistical error of the photometry was larger than 10% of the signal. We named that height z_c. Then, for every height, the photometry was obtained by averaging over the range of heights $z - p\,z/z_c \leqslant z \leqslant z + p\,z/z_c$, where $p = 0\farcs75$ is the pixel size. Thus, smoothing was small close to the midplane ($z < z_c$), but significant for low signal-to-noise regions, where $z \geqslant z_c$.

3.3. Comparison between Observed and Synthetic Luminosity Profiles

Both synthetic and observed luminosity profiles were scaled in the same way before the actual fitting. In both cases, the midplane surface brightness was set to be one. In CO11b, we had stretched the z-axis in such a way that the surface brightness at $z = 200$ was equal to one-tenth of the surface brightness at $z = 0$, $I(z = 200) = 0.1I(z = 0)$. Thus, the synthetic and the observed luminosity were forced to intersect at the point for which the luminosity is one-tenth of the midplane one. In the present paper, we made four different vertical scalings, $I(z = 200) = 0.1I(z = 0)$, $I(z = 200) = 0.2I(z = 0)$, $I(z = 200) = 0.3I(z = 0)$, and $I(z = 200) = 0.4I(z = 0)$. For practical purposes, what this stretching does is to set the luminosity at which the synthetic and the observed luminosity profiles intersect. The synthetic fits were convolved with a Gaussian kernel with an FWHM of $2\farcs2$, which is the approximate FWHM of both 3.6 and 4.5 μm band S^{4}G point-spread functions (PSFs) made by stacking several hundreds non-saturated stars (S^{4}G "super-PSF"; Sheth et al. 2010).

The fitting of the observed luminosity profiles was done by following the procedure described in Section 3.5 and Figure 4 in CO11b. Basically, after being scaled, the observed luminosity profiles for each radial bin in each galaxy were compared to the grid of synthetic models. That was done by minimizing the differences of the brightest section of the profiles starting at a dynamic range of $\Delta m = 4.5$ mag arcsec^{-2} and then going to fainter levels in steps of 0.5 mag arcsec^{-2} down to 28 mag arcsec^{-2}. We selected as the "correct" fit the one with the largest Δm having a $\chi^2 < 0.01$ (mag arcsec^{-2})^2, where χ^2 is the mean-squared difference in magnitudes between both profiles. This procedure was only done down to 26 mag arcsec^{-2} in CO11b. The lower fitted surface brightness for a given fit is μ_1 and the midplane luminosity is μ_0. Thus, for a given fit, the dynamical range Δm over which a fit has been produced is $\Delta m = \mu_1 - \mu_0$. μ_1 is reached at a height z_1, which is typically on the order of the smoothing scale height, z_c.

In some cases, no $\chi^2 < 0.01$ (mag arcsec^{-2})^2 fit was found for a given bin and thus this bin was flagged to be non-fittable.

The code also includes a module for computing the effect of some dust absorption in the midplane as described in CO11b.

An example of a vertical luminosity profile fit is presented in Figure 1 and all the vertical luminosity profiles for our final sample galaxies appear in Figure 17. The errors in the photometric profile depict the statistical error of the averaging used at obtaining each photometric point. In spite of the care which has been taken at determining the background level, several profiles show a significant flux at a large height (at a level of ~27–26 mag arcsec^{-2}). There are several possible explanations for this: in some cases, the galaxies are surrounded by a crowd of globular clusters and/or foreground stars whose extended wings are hard to distinguish from thick disk light and may have not been properly masked. In the case of galaxies with a larger angular size, large-scale background variations as those described in Comerón et al. (2011c) may be present and may cause artifacts in some profiles. Also, large saturated stars affect some of the profiles. Finally, some galaxies may have faint extended halos at a brightness level comparable to our detection threshold. The restrictions applied to choosing the right fits (mainly selecting as good fits those with $\chi^2 < 0.01$ (mag arcsec^{-2})^2) preclude this residual light from affecting our results.

3.4. Determination of the Height above Which the Thick Disk Dominates the Luminosity Profile

A key parameter needed for producing the luminosity profiles of the thin and thick disks parallel to midplanes is the range of heights for which each disk dominates the light emission. We defined z_s to be the height above which a fraction $f_T = 90\%$ of the light is emitted by the thick disk according to the fits to the vertical luminosity profiles. This value was calculated for each of the correctly fitted bins.

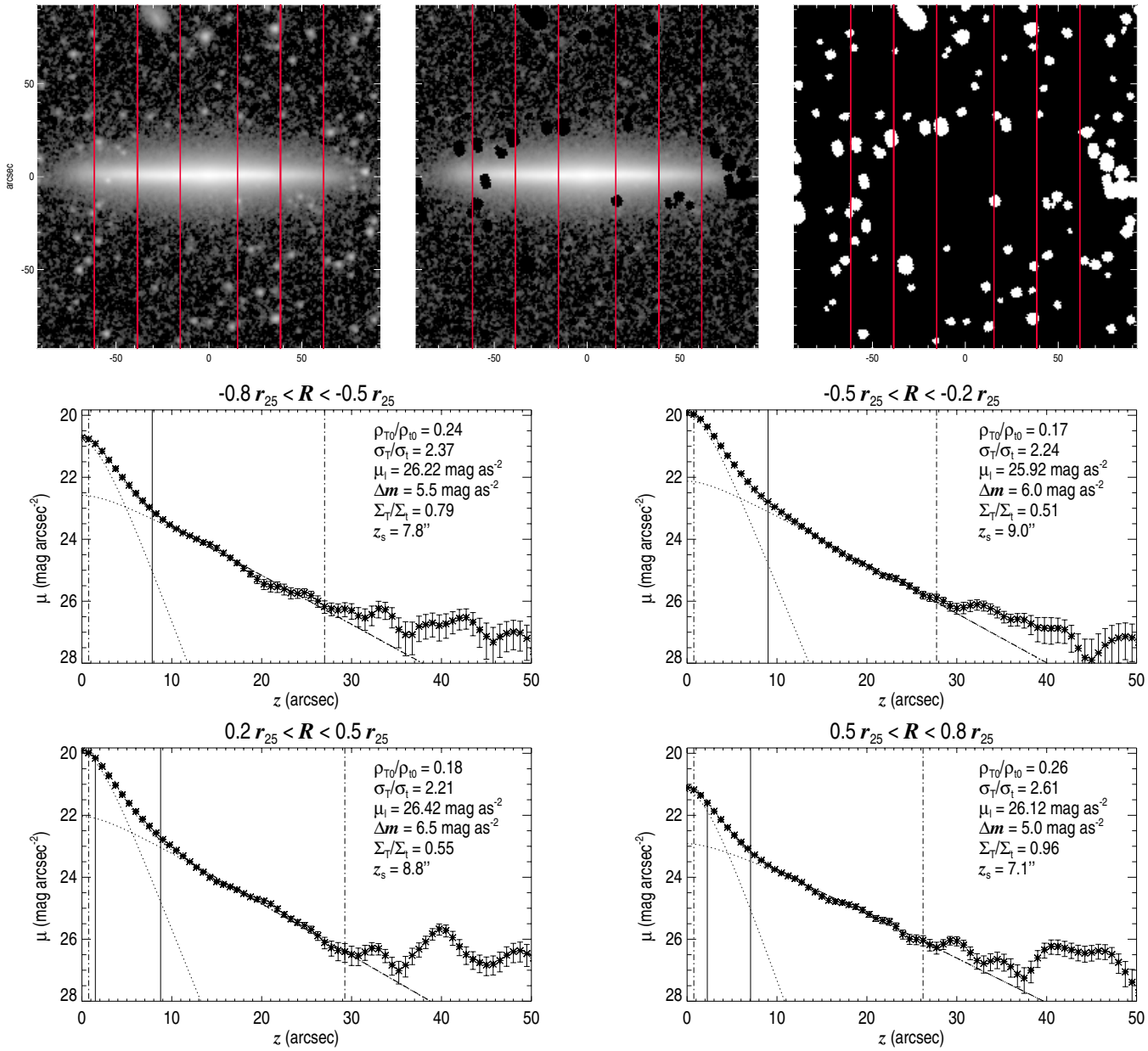

Figure 1. Vertical luminosity profile fit for NGC 5470. The three images in the top row show the average of the 3.6 and 4.5 μm band background-subtracted S^{4}G frames (left), the same image after masking (center), and the used mask (right). The vertical red lines indicate the limits of the fitted vertical bins, the central one being ignored due to the possible presence of a bulge. The other panels show the fits to the luminosity profiles in these bins. The data points have 2σ statistical error bars, the dashed curve represents the best fit, the dotted curves indicate the contributions of the thin and thin disks. The dash-dotted vertical lines indicate the limits of the range in vertical distance above the mid-plane used for the fit. The vertical solid line indicates z_s for each bin.

(A color version of this figure is available in the online journal.)

In the example fit presented in Figure 1, the z_s for each bin is indicated by a solid vertical line in each of the middle and lower row panels.

3.5. Selection of Reliable Vertical Luminosity Profile Fits

In order for a fit made for a given bin in a given galaxy to be further considered for use in this paper, several conditions were implemented.

1. A few galaxies, such as NGC 4013, have relatively bright components in addition to the thin and thick disks (CO11b; Comerón et al. 2011a). These components are likely to be a second thick disk or a bright-squashed halo. In order to avoid including galaxies with wrong fits due to these components, we excluded fits for which $\mu_1 < 24.5$ mag arcsec^{-2}. This threshold ensures that, for most cases, possible additional components are dim enough not to significantly affect the fit.
2. The statistical uncertainties for fits made in very faint galaxies are large. To minimize this problem, we have only flagged as valid those fits for which the midplane surface brightness is $\mu_0 < 22$ mag arcsec^{-2}.
3. In a few cases, as described in CO11b, the fit is compatible with a single disk. This is most likely to happen for the fits done over a small Δm, for which the fitted dynamical range is not large enough to allow distinguishing between both disks. We rejected fits compatible with a single disk. The criterion to detect those fits is slightly more restrictive

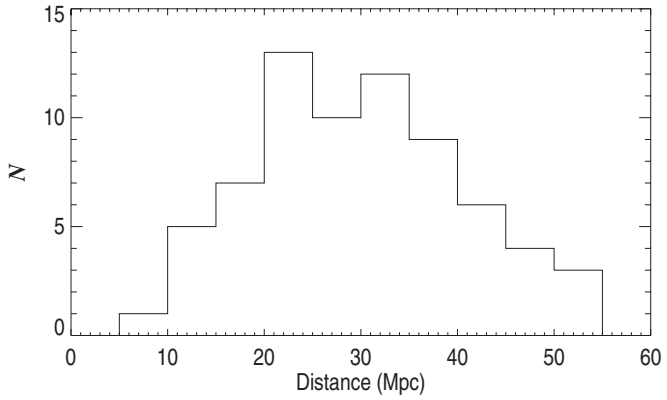

Figure 2. Histogram of the distances of the 70 galaxies in our final sample.

than in CO11b, namely, that the mean-squared difference between the fitted solution and a single-disk profile is $\chi^2 < 0.5\,(\mathrm{mag\,arcsec^{-2}})^2$.

One of our assumptions when producing the fits is that the scale lengths of both the thin and thick disks are similar and that their scale heights do not vary too much with radius. This implies that z_s should be roughly constant with the projected radius, R. As a final quality check for our fits, we selected those galaxies having more than one radial bin with a "good" fit according to the criteria expressed in the list and we looked for the largest and smallest z_s among those fits. If the ratio between these two was smaller than 1.5, then the galaxy was included in the final sample. If the ratio was larger than 1.5, then the galaxy was only included if the two $0.2r_{25} < |R| < 0.5r_{25}$ bins had a "good" fit and the ratio between their z_s was smaller than 1.5. The fits for the bins with $0.5r_{25} < |R| < 0.8r_{25}$ were then rejected and only those with $0.2r_{25} < |R| < 0.5r_{25}$ were considered when measuring the global properties of the galaxy (such as the average z_s and the disk relative masses, M_T/M_t). This was the case for 10 galaxies and was made so as not to exclude those galaxies with flares or truncations potentially happening at $0.5r_{25} < |R| < 0.8r_{25}$ or galaxies with noisy profiles at this range of projected radii.

Galaxies with varying z_s (and thus excluded from the final sample) do not necessarily have intrinsically largely varying scale lengths. For example, in the case of galaxies with a small angular size, they are likely to have a foreground star or a globular cluster covering a large fraction of the fitting bin at some height. In some cases, masking those features may be as harmful for the vertical luminosity profiles as not masking them at all, because it will cause different heights to have their surface brightness measured in significantly different ranges of projected radii. This would result in unreliable fits which are excluded by the z_s stability criterion.

The z_s stability selection criterion is also useful for removing galaxies whose thin disk is so thin that it is barely or not resolved.

Applying all these criteria trimmed the original sample from 169 to 70 galaxies. The properties of these 70 galaxies are presented in Table 1. These restrictive criteria cause 11 out of 30 galaxies included in the CO11b final sample not to appear in this paper. Fits in galaxies of the final sample which have not been used are labeled as "Not used" in Figure 17. The distance distribution of the 70 selected galaxies is presented in Figure 2. The median distance of the sample is 29.8 Mpc.

For each of the 70 galaxies in our sample, as done in CO11b, the vertical luminosity profile fits were used for estimating the ratio of the stellar mass of the thick and the thin disk for each

Table 1
Properties of the 70 Galaxies in Our Final Sample

Galaxy ID	T	Distance (Mpc)	B (mag)	v_c km s^{-1}	r_{25} ($''$)	P.A. ($^\circ$)
ESO 157-049	3.0	23.9	13.55	90.48	52	28.1
ESO 240-011	4.8	42.4	11.52	267.46	16	127.2
ESO 292-014	6.5	24.9	12.47	107.73	89	83.9
ESO 346-001	5.1	34.9	13.29	47.68	64	64.3
ESO 440-027	6.6	21.6	11.50	117.53	10	79.7
ESO 443-021	5.8	48.1	13.24	161.71	37	159.3
ESO 466-014	3.8	47.7	14.23	121.00	40	50.4
ESO 469-015	3.3	27.0	13.69	93.01	56	149.6
ESO 533-004	5.2	36.2	13.05	147.54	55	150.5
ESO 544-027	3.4	40.3	14.20	92.00	46	153.3
IC 0217	5.9	24.2	13.86	100.15	60	35.7
IC 0610	3.9	20.7	13.44	133.84	57	29.0
IC 1197	6.0	25.7	13.14	87.90	77	56.4
IC 1553	5.2	39.9	13.38	67.93	40	15.0
IC 1711	3.0	52.3	13.19	173.41	75	43.9
IC 1913	3.4	21.4	13.38	77.88	58	147.7
IC 2058	6.5	19.4	12.13	82.78	102	17.4
IC 2135	6.0	29.2	11.93	107.08	97	108.6
IC 5176	4.5	26.4	12.02	164.38	134	27.9
NGC 0489	2.7	33.5	12.42	180.91	46	120.8
NGC 0522	4.1	35.0	12.28	169.10	72	32.9
NGC 0678	3.0	27.1	12.15	169.03	93	77.4
NGC 1032	0.4	35.6	12.13	283.94	106	67.5
NGC 1163	4.1	30.9	13.40	142.07	69	143.0
NGC 1422	2.3	16.9	13.22	65.87	75	65.5
NGC 1495	5.0	17.3	12.19	90.73	67	104.5
NGC 1596	−2.0	15.6	11.94	98.32	117	18.7
NGC 2732	−2.0	31.8	12.73	32.30	55	65.7
NGC 3098	−1.5	22.4	12.68	129.73	70	88.7
NGC 3279	6.5	32.5	12.37	155.85	74	152.0
NGC 3454	5.5	21.3	12.44	91.25	72	116.1
NGC 3501	5.9	23.3	12.09	133.61	128	28.0
NGC 3592	5.3	22.7	13.44	79.72	64	117.7
NGC 3600	1.0	13.6	12.78	86.90	56	4.4
NGC 3628	3.1	12.2	9.150	215.16	329	102.6
NGC 4081	1.0	26.1	15.12	116.53	42	130.0
NGC 4111	−1.4	16.0	11.60	71.63	53	152.2
NGC 4330	6.3	19.5	11.99	117.85	69	59.2
NGC 4359	5.0	13.3	13.43	102.83	41	107.7
NGC 4437	6.0	9.8	9.620	140.13	274	82.4
NGC 4565	3.2	13.3	8.970	244.94	498	135.1
NGC 4607	3.4	20.0	12.63	98.93	87	2.7
NGC 4747	7.2	12.3	12.36	69.60	63	31.9
NGC 5084	−2.0	26.4	11.07	309.88	300	81.0
NGC 5470	3.1	18.0	13.00	109.45	77	62.2
NGC 5529	5.3	50.0	11.20	284.14	173	114.3
NGC 5981	4.3	29.2	12.48	251.12	83	139.8
NGC 6010	0.4	21.6	12.33	148.80	55	103.3
NGC 7347	4.6	38.7	13.25	115.11	46	130.8
PGC 013646	5.1	32.6	12.32	168.16	102	34.4
PGC 028308	6.8	40.5	12.87	167.27	60	125.8
PGC 030591	6.8	29.8	13.36	111.59	45	168.4
PGC 032548	−0.2	37.3	15.06	93.33	27	149.7
PGC 052809	5.9	24.9	12.46	100.97	95	169.2
UGC 00903	3.9	51.6	13.09	163.23	50	52.6
UGC 01970	5.9	33.9	13.32	95.20	55	22.5
UGC 05347	6.5	33.8	13.53	95.64	41	17.0
UGC 05689	6.4	43.4	14.07	119.67	40	153.4
UGC 05958	4.0	29.4	14.26	78.15	49	178.9
UGC 06526	7.0	32.3	12.64	72.57	49	87.2
UGC 07086	3.1	32.8	14.02	126.01	69	70.5
UGC 08737	4.0	41.9	13.27	163.31	72	150.7
UGC 09448	3.2	37.8	13.95	111.50	49	85.8
UGC 09665	4.0	42.5	13.57	126.05	51	141.5

Table 1
(Continued)

Galaxy ID	T	Distance (Mpc)	B (mag)	v_c km s^{-1}	r_{25} ($''$)	P.A. ($^\circ$)
UGC 10043	4.1	37.3	13.80	143.59	66	150.5
UGC 10288	5.3	32.4	12.09	166.59	144	90.4
UGC 10297	5.1	39.2	13.43	102.82	64	2.9
UGC 12518	3.0	51.6	14.11	49.58	42	25.2
UGC 12692	3.9	49.6	14.21	101.34	38	53.2
UGC 12857	4.0	34.5	13.24	107.94	61	33.5

Notes. T values from HyperLEDA. Distance values from the average of redshift-independent measurements in NED when available and, if not, from Virgo Infall corrected radial velocities and a Hubble-Lemaître constant $H_0 = 73\,\mathrm{km\,s^{-1}\,Mpc^{-1}}$. B values are HyperLEDA's internal absorption-corrected values. v_c values from HyperLEDA. r_{25} values from HyperLEDA except for NGC 4111, for which we used the RC3 value. P.A. values from HyperLEDA, except for ESO 440-027, IC 5176, and NGC 3098, for which we measured our own P.A. values using ellipse fitting.

galaxy, M_T/M_t, using the following expression:

$$\frac{M_T}{M_t} = \frac{\sum_b \left(10^{-0.4\mu_{0b}}\right)(\Sigma_T/\Sigma_t)_b}{\sum_b 10^{-0.4\mu_{0b}}}, \quad (2)$$

where Σ_i refers to the edge-on column mass densities, the subindex b refers to the different bins in galactocentric distance for which "good" fits have been obtained, and μ_0 is the midplane surface brightness for a given bin in magnitudes.

3.6. Observed Luminosity Profiles Parallel to Galaxy Midplanes

For each galaxy in our final 70 galaxy sample, we obtained a single height above which the thick disk dominates the luminosity, the global galaxy z_s, by averaging the local z_s values in all of the bins with valid fits. We also calculated z_u, which is the height at which the 26 mag arcsec^{-2} level was found averaged over the valid fits. The z_s and z_u values are listed in Table 2.

The region dominated by the thin disk was defined to be that between $z = 0$ and $z = 0.5z_s$ at all projected radii, R, in accordance with the assumption of roughly constant scale heights for all disks. The region dominated by the thick disk was defined to be that between $z = z_s$ and $z = z_u$ at all projected radii. We averaged the galaxy over its four quarters (top right, top left, bottom left, and bottom right), taking into account the masking and using for the P.A. of the disk major axis the value appearing in HyperLEDA, except for a few cases for which that value was obviously off by a few degrees, where we used our own value for the disk P.A. computed using ellipse fitting.

We used the average of the four quarters of the galaxy to obtain a luminosity profile parallel to the midplane for both the thin (thin horizontal profile) and the thick disk (thick horizontal profile) by averaging in z over the range of heights they dominate. We produced a third luminosity profile including the light of both the thin and the thick disk by averaging the light from $z = 0$ to $z = z_u$ (total horizontal profile).

In order to increase the signal to noise in the outer parts of the galaxy, we used a logarithmic sampling; each data point was measured at a radial distance 1.03 times larger than the previous one. For each of the three horizontal profiles, we calculated the projected radius at which the 27 mag arcsec^{-2} level is found. We defined R_f to be the largest of these projected radii and we cut the three profiles down to R_f.

Table 2
z_s and z_u Values

ID	z_s ($''$)	z_u ($''$)	ID	z_s ($''$)	z_u ($''$)
ESO 157-049	6.8	23.2	NGC 4081	8.9	33.5
ESO 240-011	17.4	31.9	NGC 4111	25.4	52.3
ESO 292-014	8.3	23.1	NGC 4330	10.1	34.6
ESO 346-001	6.6	14.9	NGC 4359	12.7	48.4
ESO 440-027	10.4	40.6	NGC 4437	40.8	83.8
ESO 443-021	10.7	23.0	NGC 4565	42.3	109.7
ESO 466-014	6.3	16.2	NGC 4607	7.6	32.3
ESO 469-015	6.7	21.1	NGC 4747	9.8	61.4
ESO 533-004	6.9	22.2	NGC 5084	17.5	144.7
ESO 544-027	6.0	18.8	NGC 5470	8.4	27.8
IC 0217	9.0	26.5	NGC 5529	10.1	26.0
IC 0610	7.1	24.1	NGC 5981	11.4	28.4
IC 1197	5.7	23.3	NGC 6010	16.0	41.7
IC 1553	9.1	24.2	NGC 7347	10.9	20.9
IC 1711	10.8	30.3	PGC 013646	11.6	25.1
IC 1913	12.4	20.0	PGC 028308	8.0	22.3
IC 2058	7.4	21.6	PGC 030591	8.3	16.5
IC 2135	6.9	32.3	PGC 032548	6.9	15.0
IC 5176	10.7	41.4	PGC 052809	8.0	30.9
NGC 0489	10.8	22.5	UGC 00903	7.8	33.3
NGC 0522	8.8	26.4	UGC 01970	10.	23.1
NGC 0678	22.2	55.7	UGC 05347	9.2	14.0
NGC 1032	28.7	75.2	UGC 05689	7.3	21.1
NGC 1163	7.7	23.7	UGC 05958	6.7	16.6
NGC 1422	9.7	34.0	UGC 06526	7.7	21.0
NGC 1495	11.2	27.7	UGC 07086	6.7	31.0
NGC 1596	21.7	81.4	UGC 08737	6.4	27.3
NGC 2732	10.9	38.7	UGC 09448	7.4	18.2
NGC 3098	8.6	33.1	UGC 09665	10.3	23.5
NGC 3279	9.3	26.0	UGC 10043	6.1	17.5
NGC 3454	10.2	29.2	UGC 10288	8.8	32.4
NGC 3501	12.0	27.0	UGC 10297	12.4	16.2
NGC 3592	8.8	23.5	UGC 12518	6.8	21.2
NGC 3600	12.8	40.7	UGC 12692	8.0	21.6
NGC 3628	20.0	140.5	UGC 12857	13.1	26.1

The horizontal luminosity profiles are displayed in the bottom panels of Figure 17.

3.7. Fitting of the Horizontal Luminosity Profiles

Erwin et al. (2008) described breaks in disks by using what they termed the "broken-exponential" function which consists of two exponential pieces joined by a transition of variable "sharpness" (their Equation (5)). We generalized this function to allow us to describe profiles with more than one break (both truncations and antitruncations):

$$I(r) = S\, I_0\, e^{-\frac{r}{h_1}} \prod_{i=2}^{i=n} \left\{ \left[1 + e^{\alpha_{i-1,\mathrm{i}}(r - r_{i-1,\mathrm{i}})}\right]^{\frac{1}{\alpha_{i-1,\mathrm{i}}}\left(\frac{1}{h_{i-1}} - \frac{1}{h_i}\right)} \right\}, \quad (3)$$

where S is a scaling factor defined as

$$S^{-1} = \prod_{i=2}^{i=n} \left\{ \left[1 + e^{-\alpha_{i-1,\mathrm{i}}\, r_{i-1,\mathrm{i}}}\right]^{\frac{1}{\alpha_{i-1,\mathrm{i}}}\left(\frac{1}{h_{i-1}} - \frac{1}{h_i}\right)} \right\}. \quad (4)$$

I_0 stands for the central brightness of the inner exponential section, r for the radial distance, h_i for the scale lengths of the different sections, n is the number of exponential sections in the profile, $r_{i-1,\mathrm{i}}$ stands for the break radius between the section

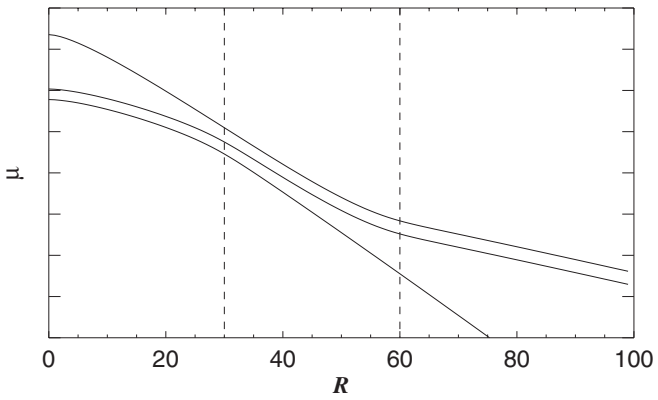

Figure 3. Examples of a profile with an antitruncation (top; Type III profile), with a truncation and antitruncation (middle; Type II+III profile), and a truncation (bottom; Type II profile). All profiles have been obtained using Equation (6). For the top profile, the antitruncation radius is $r_{1,2} = 60$ and the scale lengths are $h_1 = 10$ and $h_2 = 30$. For the middle profile the break radii are $r_{1,2} = 30$ and $r_{2,3} = 60$ and the scale lengths are $h_1 = 20$, $h_1 = 10$, and $h_3 = 30$. For the bottom profile the truncation radius is $r_{1,2} = 30$ and the scale lengths are $h_1 = 20$ and $h_2 = 10$. The dotted vertical lines indicate the break radii. I_0 values have been set arbitrarily.

with an h_{i-1} slope and that with an h_i slope, and $\alpha_{i-1,\mathrm{i}}$ is a parameter which controls the sharpness of the breaks.

For profiles with no breaks we used a simple exponential:

$$I(r) = I_0\, e^{-\frac{r}{h_1}}. \quad (5)$$

Equations (3) and (5) cannot be immediately applied for the fitting of horizontal luminosity profiles because they need to be integrated along the line of sight. We did so assuming that the galaxy had a sharp cutoff at $r_f = 5\,R_f$, although the results do not depend on this cutoff radius as long it is large enough ($r_f \gtrapprox 1.5\,R_f$). So, if we define s to be $s \equiv \sqrt{r^2 - R^2}$, then the integral along the line of sight is

$$J(R) = 2\int_{s=0}^{s=s_f} I\left(\sqrt{R^2 + s^2}\right) ds, \quad (6)$$

where $s_f = \sqrt{R_f^2 - R^2}$.

Since the result of Equation (6) yields non-analytic results, we fitted our luminosity profile data in magnitudes with $-2.5\log(J(R))$ using IDL's CURVEFIT function. For each fit, the number of truncations, n, was manually set after observing the luminosity profiles. The initial values for the scale lengths were those obtained from an exponential fit to each of the exponential sections. We found that, especially for profiles with more than two breaks, the number of fitting parameters was too high to yield reliable results, so we set all $\alpha_{\mathrm{i}-1,\mathrm{i}} = 0.5$, which is typical of break sharpnesses found in Erwin et al. (2008).

The fitting range was set manually by defining the limits that we called $R_{\min}$ and $R_{\max}$. Special care was taken in order to exclude regions strongly affected by bulges and noisy outskirt regions from the fitting range.

Examples of Equation (3) integrated over the line of sight are presented in Figure 3. The top and the bottom profile represent an antitruncated and a truncated profile, respectively. The middle profile combines the breaks of the two other profiles. Due to line of sight integration, the profiles do not have a central peak and have a rounded profile for $R \ll h_1$.

The fits to the horizontal luminosity profiles are overlaid to the profiles in Figure 17 (black lines). The fitted parameters for total, thin, and thick disk profiles are presented in Tables 3, 4, and 5, respectively.

4. WHAT IF FITS WERE DONE IN GALAXIES NOT FULFILLING OUR ASSUMPTIONS?

Throughout the fitting process, several assumptions were made. Deviations from these perfect conditions should be tested in order to know whether our results are accurate.

Two parameters from our fits are especially important for our conclusions (and those in CO11b): the ratio of the stellar masses of the thick and the thin disk, M_T/M_t, and z_s, which needs to be precisely measured so as to obtain a correct separation of the light of the thin and the thick disk. M_T/M_t was measured by averaging the ratio of the thick and thin disk edge-on column mass densities, Σ_T/Σ_t, over all the bins with "good" vertical luminosity fits (Equation (2)).

We thus have to test the reliability of the fitted values of z_s and Σ_T/Σ_t if we loosen some of our assumptions.

1. What happens if the scale lengths of the thin and thick disks are not similar?
2. What happens if the scale lengths of the disks are not constant and a disk has breaks?
3. What happens if the disk is sub-maximal and thus dominated by dark matter within the optical radius?
4. What happens if the disk of a galaxy is not as edge-on as we think it is?
5. We computed our results for the case $\Upsilon_T/\Upsilon_t = 1.2$. We know from CO11b that Σ_T/Σ_t roughly scales with Υ_T/Υ_t for reasonable star formation histories, but would z_s remain unchanged if we had selected the wrong Υ_T/Υ_t?
6. We assumed the gas column mass density to scale with that of the thin disk, thus ensuring constant scale heights for all disks. However, Bigiel et al. (2008) have showed that in spiral galaxies, molecular gas tends to concentrate in the central parts of the galaxy. Their data also show that the atomic gas column mass density within r_{25} varies little with radius and that it dominates the gas column density for $r > 0.5r_{25}$. What would happen if the gas distribution was significantly different from the one assumed?

4.1. A Galaxy Model in Order to Test Deviations from Our Assumptions

A set of model galaxies was created in order to test the result of loosening our assumptions when producing the fits to vertical luminosity profiles. The model galaxies were considered to have $r_{25} = 9.2$ kpc, and an inner thin disk scale length $h_{\mathrm{t1}} = 0.3r_{25}$, which is the median value in our final 70 galaxy sample. In case of truncated thin disks, the scale length of the outer section has been set to be $h_{\mathrm{t2}} = 0.12r_{25}$, which again is typical of what is observed in our galaxies. We designed all model galaxies to have a stellar face-on column mass density equal to $S = S_t + S_T = 60\,M_\odot\,\mathrm{pc}^{-2}$ and a thin disk vertical velocity dispersion $\sigma_t = 20\,\mathrm{km\,s}^{-1}$ at $r = 0.65r_{25}$, which is on the order of what is found in the solar neighborhood. The absolute value of the column mass density and the velocity dispersion are only relevant when considering the biases due to the gas distribution and the dark matter halo, which, as seen later, are small compared to those caused by the inclination angle, the thick disk relative scale length, and the thick disk column mass density. The truncations in disks were described using Equation (3).

Table 3
Results of the Fits to Horizontal Luminosity Profiles for the Whole Disk

ID	Type	I_0 (mag as^{-3})	r_i ($''$)	r_o ($''$)	h ($''$)
ESO 157-049	Type II+III	24.81 ± 0.29	4.0 ± 0.0	24.7 ± 3.4	24.6 ± 12.7
			24.7 ± 3.4	48.9 ± 4.2	6.7 ± 0.7
			48.9 ± 4.2	72.4 ± 0.0	14.7 ± 1.9
ESO 240-011	Type II	25.11 ± 0.08	11.7 ± 0.0	89.4 ± 39.3	29.2 ± 1.3
			89.4 ± 39.3	197.8 ± 0.0	27.0 ± 0.7
ESO 292-014	Type II	25.60 ± 0.09	13.9 ± 0.0	80.5 ± 4.2	20.2 ± 0.8
			80.5 ± 4.2	87.9 ± 0.0	7.1 ± 1.9
ESO 346-001	Type II+II	25.43 ± 0.12	7.6 ± 0.0	23.5 ± 3.2	21.3 ± 3.2
			23.5 ± 3.2	53.6 ± 4.4	11.1 ± 0.7
			53.6 ± 4.4	59.0 ± 0.0	5.9 ± 1.4
ESO 440-027	Type II+III	26.81 ± 0.42	24.3 ± 0.0	57.6 ± 11.9	51.3 ± 26.3
			57.6 ± 11.9	124.8 ± 17.5	23.8 ± 1.9
			124.8 ± 17.5	172.9 ± 0.0	34.6 ± 4.0
ESO 443-021	Type II	24.73 ± 0.22	11.7 ± 0.0	37.7 ± 2.8	18.0 ± 3.0
			37.7 ± 2.8	66.8 ± 0.0	8.2 ± 0.3
ESO 466-014	Type II	24.65 ± 0.17	1.5 ± 0.0	18.8 ± 3.5	11.4 ± 2.0
			18.8 ± 3.5	47.5 ± 0.0	6.7 ± 0.2
ESO 469-015	Type II+III	24.64 ± 0.26	1.5 ± 0.0	9.2 ± 1.9	114.4 ± 382.6
			9.2 ± 1.9	27.1 ± 1.8	4.7 ± 0.4
			27.1 ± 1.8	59.0 ± 0.0	14.9 ± 0.9
ESO 533-004	Type II	25.10 ± 0.22	12.8 ± 0.0	38.5 ± 3.2	24.0 ± 4.2
			38.5 ± 3.2	87.9 ± 0.0	11.1 ± 0.2
ESO 544-027	Type II	24.74 ± 0.39	2.3 ± 0.0	12.3 ± 4.9	18.9 ± 24.4
			12.3 ± 4.9	49.6 ± 0.0	7.4 ± 0.2
IC 0217	Type II	26.06 ± 0.22	7.6 ± 0.0	25.3 ± 4.1	33.9 ± 14.6
			25.3 ± 4.1	91.3 ± 0.0	15.1 ± 0.2
IC 0610	Type II+II	25.24 ± 0.18	11.7 ± 0.0	25.1 ± 2.7	48.0 ± 19.8
			25.1 ± 2.7	48.2 ± 7.6	10.8 ± 1.2
			48.2 ± 7.6	69.5 ± 0.0	8.2 ± 0.5
IC 1197	Type II	26.72 ± 0.22	9.6 ± 0.0	41.8 ± 4.5	38.5 ± 13.4
			41.8 ± 4.5	98.4 ± 0.0	15.3 ± 0.4
IC 1553	Type II+III	24.26 ± 0.07	7.6 ± 0.0	29.4 ± 0.2	11.7 ± 0.3
			29.4 ± 0.2	32.8 ± 0.2	1.6 ± 0.1
			32.8 ± 0.2	49.6 ± 0.0	10.8 ± 0.8
IC 1711	Type II	26.76 ± 0.13	28.9 ± 0.0	69.7 ± 3.9	25.9 ± 1.6
			69.7 ± 3.9	87.9 ± 0.0	12.6 ± 1.2
IC 1913	Type II	27.36 ± 0.20	17.6 ± 0.0	34.2 ± 2.9	43.6 ± 13.6
			34.2 ± 2.9	69.5 ± 0.0	12.0 ± 0.5
IC 2058	Type II	26.29 ± 0.06	1.5 ± 0.0	90.5 ± 6.9	26.1 ± 0.9
			90.5 ± 6.9	118.0 ± 0.0	15.7 ± 1.5
IC 2135	Type II	26.10 ± 0.18	13.9 ± 0.0	68.2 ± 4.4	41.0 ± 7.1
			68.2 ± 4.4	122.3 ± 0.0	15.4 ± 0.6
IC 5176	Type III	24.22 ± 0.06	4.9 ± 0.0	75.0 ± 3.2	16.2 ± 0.4
			75.0 ± 3.2	172.9 ± 0.0	32.0 ± 0.8
NGC 0489	Type I	23.01 ± 0.11	4.9 ± 0.0	56.6 ± 0.0	7.6 ± 0.2
NGC 0522	Type II+III	25.75 ± 0.10	12.8 ± 0.0	54.4 ± 1.3	44.5 ± 5.2
			54.4 ± 1.3	102.2 ± 6.0	8.9 ± 0.4
			102.2 ± 6.0	98.4 ± 0.0	94.5 ± 88.5
NGC 0678	Type II	31.81 ± 0.38	49.6 ± 0.0	118.0 ± 2.1	−43.6 ± 8.4
			118.0 ± 2.1	140.8 ± 0.0	12.0 ± 1.0
NGC 1032	Type II	27.36 ± 0.04	47.5 ± 0.0	131.7 ± 11.1	39.6 ± 0.6
			131.7 ± 11.1	185.0 ± 0.0	31.8 ± 1.4
NGC 1163	Type II+III	24.50 ± 0.33	5.7 ± 0.0	14.4 ± 7.8	14.4 ± 7.8
			14.4 ± 7.8	42.2 ± 3.3	9.1 ± 0.8
			42.2 ± 3.3	98.4 ± 0.0	18.9 ± 0.7

Table 3
(Continued)

ID	Type	I_0 (mag as^{-3})	r_i ($''$)	r_o ($''$)	h ($''$)
NGC 1422	Type III	25.48 ± 0.09	4.0 ± 0.0	49.1 ± 3.2	13.1 ± 0.6
			49.1 ± 3.2	118.0 ± 0.0	30.2 ± 1.2
NGC 1495	Type II	25.35 ± 0.13	27.3 ± 0.0	93.1 ± 7.5	21.2 ± 0.9
			93.1 ± 7.5	113.8 ± 0.0	12.9 ± 1.8
NGC 1596	Type III	26.21 ± 0.10	27.3 ± 0.0	152.5 ± 7.9	27.6 ± 0.9
			152.5 ± 7.9	241.0 ± 0.0	107.1 ± 17.6
NGC 2732	Type II	24.33 ± 0.03	10.6 ± 0.0	49.9 ± 3.0	13.1 ± 0.2
			49.9 ± 3.0	78.3 ± 0.0	10.5 ± 0.2
NGC 3098	Type III	23.94 ± 0.13	27.3 ± 0.0	75.9 ± 8.5	11.8 ± 0.4
			75.9 ± 8.5	91.3 ± 0.0	18.1 ± 3.6
NGC 3279	Type II	25.00 ± 0.11	0.0 ± 0.0	35.4 ± 2.3	35.2 ± 6.5
			35.4 ± 2.3	94.8 ± 0.0	12.6 ± 0.2
NGC 3454	Type II+III	26.42 ± 0.13	4.9 ± 0.0	39.4 ± 1.9	58.6 ± 18.9
			39.4 ± 1.9	47.3 ± 2.4	5.0 ± 1.7
			47.3 ± 2.4	94.8 ± 0.0	18.5 ± 0.7
NGC 3501	Type II	25.15 ± 0.12	27.3 ± 0.0	96.0 ± 6.3	24.6 ± 1.2
			96.0 ± 6.3	135.9 ± 0.0	15.9 ± 0.8
NGC 3592	Type II	25.57 ± 0.12	11.7 ± 0.0	59.1 ± 6.9	16.3 ± 0.9
			59.1 ± 6.9	75.3 ± 0.0	10.5 ± 1.3
NGC 3600	Type III	26.33 ± 0.00	24.3 ± 0.0	71.1 ± 0.0	17.6 ± 0.0
			71.1 ± 0.0	118.0 ± 0.0	43.9 ± 0.0
NGC 3628	Type II+III+II	26.70 ± 0.08	59.0 ± 0.0	167.9 ± 3.1	94.6 ± 5.8
			167.9 ± 3.1	187.0 ± 2.7	18.5 ± 2.6
			187.0 ± 2.7	356.0 ± 6.8	475.9 ± 184.4
			356.0 ± 6.8	532.0 ± 0.0	55.2 ± 1.6
NGC 4081	Type II+III	23.87 ± 0.05	0.0 ± 0.0	29.6 ± 9.2	9.4 ± 0.3
			29.6 ± 9.2	40.6 ± 4.2	7.6 ± 2.0
			40.6 ± 4.2	64.1 ± 0.0	13.8 ± 0.6
NGC 4111	Type II	25.84 ± 0.12	32.2 ± 0.0	102.7 ± 13.1	31.4 ± 1.7
			102.7 ± 13.1	145.8 ± 0.0	24.0 ± 1.4
NGC 4330	Type II+III+II	26.77 ± 0.05	15.1 ± 0.0	56.0 ± 2.0	53.3 ± 3.6
			56.0 ± 2.0	80.6 ± 1.2	18.3 ± 1.3
			80.6 ± 1.2	90.0 ± 1.4	−29.4 ± 10.7
			90.0 ± 1.4	172.9 ± 0.0	26.7 ± 0.4
NGC 4359	Type III	26.47 ± 0.06	0.0 ± 0.0	77.2 ± 6.4	20.4 ± 0.7
			77.2 ± 6.4	140.8 ± 0.0	35.5 ± 2.1
NGC 4437	Type II	27.26 ± 0.07	39.4 ± 0.0	207.5 ± 7.1	104.5 ± 5.8
			207.5 ± 7.1	389.5 ± 0.0	50.2 ± 0.8
NGC 4565	Type II+II	27.13 ± 0.19	98.4 ± 0.0	210.0 ± 20.2	133.1 ± 20.6
			210.0 ± 20.2	431.4 ± 12.3	80.4 ± 2.4
			431.4 ± 12.3	484.7 ± 0.0	43.8 ± 3.7
NGC 4607	Type II+III	25.26 ± 0.33	17.6 ± 0.0	38.4 ± 5.6	26.2 ± 8.3
			38.4 ± 5.6	58.9 ± 4.1	11.1 ± 2.1
			58.9 ± 4.1	135.9 ± 0.0	24.3 ± 0.5
NGC 4747	Type I	26.59 ± 0.05	7.6 ± 0.0	126.7 ± 0.0	27.5 ± 0.4
NGC 5084	Type III	26.65 ± 0.15	37.5 ± 0.0	170.9 ± 12.0	42.0 ± 2.8
			170.9 ± 12.0	427.9 ± 0.0	112.0 ± 5.8
NGC 5470	Type II	25.62 ± 0.07	15.1 ± 0.0	58.6 ± 1.6	26.8 ± 1.3
			58.6 ± 1.6	91.3 ± 0.0	11.0 ± 0.3
NGC 5529	Type II+III+II	25.77 ± 0.03	13.9 ± 0.0	92.5 ± 2.0	34.0 ± 0.5
			92.5 ± 2.0	139.2 ± 1.2	18.7 ± 0.4
			139.2 ± 1.2	181.7 ± 3.4	∞ ± ∞
			181.7 ± 3.4	204.5 ± 0.0	33.1 ± 3.6

Table 3
(Continued)

ID	Type	I_0 (mag as^{-3})	r_i ($''$)	r_o ($''$)	h ($''$)
NGC 5981	Type II	24.78 ± 0.22	20.2 ± 0.0	47.4 ± 5.6	21.8 ± 3.2
			47.4 ± 5.6	102.1 ± 0.0	14.4 ± 0.3
NGC 6010	Type II	25.19 ± 0.14	20.2 ± 0.0	36.0 ± 4.2	20.9 ± 2.1
			36.0 ± 4.2	94.8 ± 0.0	13.4 ± 0.3
NGC 7347	Type II	24.02 ± 0.02	13.9 ± 0.0	43.3 ± 0.5	11.0 ± 0.1
			43.3 ± 0.5	56.6 ± 0.0	5.8 ± 0.1
PGC 013646	Type II	26.24 ± 0.01	13.9 ± 0.0	52.5 ± 0.2	116.5 ± 2.2
			52.5 ± 0.2	122.3 ± 0.0	14.1 ± 0.0
PGC 028308	Type II	23.92 ± 0.09	4.9 ± 0.0	59.7 ± 10.6	10.2 ± 0.3
			59.7 ± 10.6	64.1 ± 0.0	7.2 ± 3.0
PGC 030591	Type I	24.01 ± 0.15	13.9 ± 0.0	54.2 ± 0.0	8.8 ± 0.3
PGC 032548	Type I	25.77 ± 0.00	5.7 ± 0.0	54.2 ± 0.0	10.5 ± 0.0
PGC 052809	Type II	26.07 ± 0.12	11.7 ± 0.0	72.5 ± 3.9	34.7 ± 3.3
			72.5 ± 3.9	126.7 ± 0.0	15.2 ± 0.5
UGC 00903	Type II+III	23.19 ± 0.14	4.9 ± 0.0	15.3 ± 1.9	12.8 ± 2.0
			15.3 ± 1.9	30.7 ± 2.1	5.8 ± 0.5
			30.7 ± 2.1	64.1 ± 0.0	10.8 ± 0.4
UGC 01970	Type III+II	24.70 ± 0.22	5.7 ± 0.0	20.4 ± 3.7	7.6 ± 1.1
			20.4 ± 3.7	34.0 ± 6.9	30.8 ± 26.6
			34.0 ± 6.9	78.3 ± 0.0	13.6 ± 0.4
UGC 05347	Type II	25.88 ± 0.32	6.7 ± 0.0	26.5 ± 3.8	18.0 ± 6.7
			26.5 ± 3.8	47.5 ± 0.0	7.0 ± 0.5
UGC 05689	Type II	24.81 ± 0.08	4.0 ± 0.0	20.3 ± 5.3	9.7 ± 0.5
			20.3 ± 5.3	43.3 ± 0.0	8.0 ± 0.3
UGC 05958	Type I	25.12 ± 0.15	7.6 ± 0.0	64.1 ± 0.0	10.8 ± 0.4
UGC 06526	Type III	24.42 ± 0.20	6.7 ± 0.0	34.5 ± 4.0	8.8 ± 0.8
			34.5 ± 4.0	87.9 ± 0.0	18.3 ± 0.9
UGC 07086	Type II+III	24.58 ± 0.10	0.0 ± 0.0	29.0 ± 9.6	13.1 ± 1.1
			29.0 ± 9.6	45.6 ± 5.3	9.4 ± 2.2
			45.6 ± 5.3	87.9 ± 0.0	17.9 ± 0.7
UGC 08737	Type II+III	24.75 ± 0.28	15.1 ± 0.0	28.8 ± 3.9	23.5 ± 7.3
			28.8 ± 3.9	81.8 ± 3.0	11.9 ± 0.4
			81.8 ± 3.0	122.3 ± 0.0	31.2 ± 2.7
UGC 09448	Type I	24.75 ± 0.11	8.6 ± 0.0	59.0 ± 0.0	9.6 ± 0.3
UGC 09665	Type II	24.28 ± 0.34	4.9 ± 0.0	11.3 ± 9.5	15.8 ± 9.7
			11.3 ± 9.5	59.0 ± 0.0	9.6 ± 0.4
UGC 10043	Type II	25.49 ± 0.16	18.8 ± 0.0	78.8 ± 10.2	17.2 ± 1.0
			78.8 ± 10.2	81.4 ± 0.0	4.6 ± 6.2
UGC 10288	Type II+III	26.05 ± 0.18	13.9 ± 0.0	53.3 ± 8.2	38.7 ± 7.7
			53.3 ± 8.2	127.8 ± 7.7	22.0 ± 1.1
			127.8 ± 7.7	191.3 ± 0.0	41.8 ± 3.2
UGC 10297	Type II+III	25.34 ± 0.17	0.0 ± 0.0	11.3 ± 2.9	24.3 ± 14.6
			11.3 ± 2.9	39.4 ± 2.9	8.3 ± 0.4
			39.4 ± 2.9	64.1 ± 0.0	15.0 ± 0.9
UGC 12518	Type II+III	25.29 ± 0.26	7.6 ± 0.0	19.5 ± 2.2	29.9 ± 17.0
			19.5 ± 2.2	55.0 ± 3.2	8.2 ± 0.3
			55.0 ± 3.2	72.4 ± 0.0	18.3 ± 2.7
UGC 12692	Type III	23.58 ± 0.21	7.6 ± 0.0	37.3 ± 4.4	6.1 ± 0.4
			37.3 ± 4.4	54.2 ± 0.0	14.9 ± 3.7
UGC 12857	Type I	24.62 ± 0.11	9.6 ± 0.0	66.8 ± 0.0	10.9 ± 0.3

Notes. r_i and r_o stand for the inner and the outer limit of each fitted section and h corresponds to the scale length of that section. The lower limit of the innermost section and the upper limit of the outermost section have no error bar because they have been set manually.

Table 4
Results of the Fits to Horizontal Luminosity Profiles for the Thin Disk

ID	Type	I_0 (mag as^{-3})	r_i ($''$)	r_o ($''$)	h ($''$)
ESO 157-049	Type II+III	23.14 ± 0.42	4.0 ± 0.0	23.3 ± 3.7	26.3 ± 27.1
			23.3 ± 3.7	52.9 ± 5.2	5.9 ± 0.5
			52.9 ± 5.2	69.5 ± 0.0	15.0 ± 5.1
ESO 240-011	Type II	23.86 ± 0.11	11.7 ± 0.0	100.5 ± 14.8	29.6 ± 1.7
			100.5 ± 14.8	197.8 ± 0.0	23.2 ± 0.7
ESO 292-014	Type II	23.84 ± 0.09	13.9 ± 0.0	76.8 ± 3.0	17.3 ± 0.5
			76.8 ± 3.0	87.9 ± 0.0	7.0 ± 1.0
ESO 346-001	Type II+II	24.20 ± 0.15	7.6 ± 0.0	23.0 ± 3.3	22.4 ± 4.4
			23.0 ± 3.3	52.5 ± 3.5	10.5 ± 0.7
			52.5 ± 3.5	59.0 ± 0.0	4.9 ± 1.0
ESO 440-027	Type II+III	25.20 ± 0.43	24.3 ± 0.0	64.5 ± 9.4	52.9 ± 29.8
			64.5 ± 9.4	142.3 ± 24.9	19.0 ± 1.5
			142.3 ± 24.9	172.9 ± 0.0	29.3 ± 8.9
ESO 443-021	Type II	23.41 ± 0.25	11.7 ± 0.0	36.4 ± 2.6	18.5 ± 3.5
			36.4 ± 2.6	66.8 ± 0.0	7.6 ± 0.3
ESO 466-014	Type II	23.23 ± 0.23	1.5 ± 0.0	19.5 ± 3.5	11.3 ± 2.7
			19.5 ± 3.5	47.5 ± 0.0	5.8 ± 0.2
ESO 469-015	Type II+III	22.90 ± 0.07	1.5 ± 0.0	10.2 ± 0.3	100.2 ± 70.1
			10.2 ± 0.3	25.6 ± 0.5	3.8 ± 0.1
			25.6 ± 0.5	59.0 ± 0.0	13.2 ± 0.5
ESO 533-004	Type II	23.29 ± 0.32	12.8 ± 0.0	40.6 ± 3.9	21.5 ± 5.7
			40.6 ± 3.9	87.9 ± 0.0	9.2 ± 0.3
ESO 544-027	Type II	22.94 ± 0.17	2.3 ± 0.0	14.5 ± 2.1	15.8 ± 4.5
			14.5 ± 2.1	49.6 ± 0.0	6.3 ± 0.2
IC 0217	Type II	24.12 ± 0.37	7.6 ± 0.0	34.1 ± 8.9	21.3 ± 8.1
			34.1 ± 8.9	91.3 ± 0.0	11.8 ± 0.5
IC 0610	Type II+II	23.54 ± 0.16	11.7 ± 0.0	24.9 ± 1.8	67.8 ± 34.7
			24.9 ± 1.8	50.7 ± 2.6	9.7 ± 0.7
			50.7 ± 2.6	69.5 ± 0.0	5.7 ± 0.3
IC 1197	Type II	25.22 ± 0.31	9.6 ± 0.0	44.2 ± 5.1	39.9 ± 16.6
			44.2 ± 5.1	98.4 ± 0.0	12.4 ± 0.5
IC 1553	Type II+III	22.69 ± 0.09	7.6 ± 0.0	29.5 ± 0.2	11.5 ± 0.5
			29.5 ± 0.2	32.2 ± 0.2	1.1 ± 0.1
			32.2 ± 0.2	47.5 ± 0.0	8.2 ± 0.8
IC 1711	Type II	25.18 ± 0.26	28.9 ± 0.0	79.8 ± 3.1	23.4 ± 2.7
			79.8 ± 3.1	91.3 ± 0.0	5.7 ± 1.0
IC 1913	Type II	26.46 ± 0.29	17.6 ± 0.0	35.5 ± 2.9	49.7 ± 25.8
			35.5 ± 2.9	69.5 ± 0.0	9.2 ± 0.5
IC 2058	Type II	24.91 ± 0.39	1.5 ± 0.0	37.9 ± 22.5	29.4 ± 15.9
			37.9 ± 22.5	118.0 ± 0.0	18.1 ± 1.1
IC 2135	Type II	24.17 ± 0.23	13.9 ± 0.0	68.5 ± 4.0	35.2 ± 6.7
			68.5 ± 4.0	122.3 ± 0.0	11.6 ± 0.5
IC 5176	Type III	22.18 ± 0.10	4.9 ± 0.0	71.7 ± 5.6	15.0 ± 0.6
			71.7 ± 5.6	172.9 ± 0.0	25.8 ± 0.9
NGC 0489	Type I	21.42 ± 0.11	4.9 ± 0.0	56.6 ± 0.0	6.9 ± 0.1
NGC 0522	Type II+III	24.05 ± 0.23	12.8 ± 0.0	54.9 ± 2.1	43.0 ± 12.1
			54.9 ± 2.1	88.2 ± 5.0	7.0 ± 0.5
			88.2 ± 5.0	105.9 ± 0.0	16.5 ± 4.7
NGC 0678	Type II	31.12 ± 0.55	49.6 ± 0.0	120.6 ± 2.0	−36.3 ± 8.7
			120.6 ± 2.0	150.9 ± 0.0	8.9 ± 0.6
NGC 1032	Type II	25.50 ± 0.20	47.5 ± 0.0	135.1 ± 21.8	32.3 ± 2.3
			135.1 ± 21.8	191.3 ± 0.0	24.9 ± 1.9
NGC 1163	Type II+III	22.88 ± 0.22	5.7 ± 0.0	16.8 ± 5.2	13.8 ± 3.3
			16.8 ± 5.2	40.3 ± 3.9	8.1 ± 0.9
			40.3 ± 3.9	105.9 ± 0.0	15.8 ± 0.7

Table 4
(Continued)

ID	Type	I_0 (mag as^{-3})	r_i ($''$)	r_o ($''$)	h ($''$)
NGC 1422	Type III	23.43 ± 0.16	4.0 ± 0.0	51.2 ± 4.5	10.7 ± 0.7
			51.2 ± 4.5	126.7 ± 0.0	25.3 ± 1.6
NGC 1495	Type II	23.72 ± 0.23	27.3 ± 0.0	95.2 ± 5.6	19.1 ± 1.4
			95.2 ± 5.6	113.8 ± 0.0	8.0 ± 1.3
NGC 1596	Type III	23.78 ± 0.11	27.3 ± 0.0	143.8 ± 6.3	21.2 ± 0.6
			143.8 ± 6.3	241.0 ± 0.0	57.4 ± 5.3
NGC 2732	Type II	22.77 ± 0.23	10.6 ± 0.0	28.7 ± 6.0	14.2 ± 2.3
			28.7 ± 6.0	84.6 ± 0.0	9.5 ± 0.3
NGC 3098	Type I	21.66 ± 0.18	27.3 ± 0.0	91.3 ± 0.0	10.2 ± 0.3
NGC 3279	Type II	23.38 ± 0.12	0.0 ± 0.0	36.3 ± 2.0	34.5 ± 6.5
			36.3 ± 2.0	94.8 ± 0.0	10.8 ± 0.2
NGC 3454	Type II+III	24.68 ± 0.20	4.9 ± 0.0	39.2 ± 2.6	48.7 ± 18.4
			39.2 ± 2.6	50.6 ± 3.4	5.2 ± 1.7
			50.6 ± 3.4	98.4 ± 0.0	15.6 ± 0.8
NGC 3501	Type II	23.64 ± 0.22	27.3 ± 0.0	91.5 ± 8.2	22.6 ± 1.9
			91.5 ± 8.2	145.8 ± 0.0	13.9 ± 0.7
NGC 3592	Type II	23.93 ± 0.16	11.7 ± 0.0	59.7 ± 4.8	14.3 ± 0.9
			59.7 ± 4.8	78.3 ± 0.0	7.7 ± 0.8
NGC 3600	Type I	25.51 ± 0.09	24.3 ± 0.0	118.0 ± 0.0	21.0 ± 0.4
NGC 3628	Type II+III+II	24.36 ± 0.14	59.0 ± 0.0	170.0 ± 4.2	78.6 ± 6.9
			170.0 ± 4.2	185.5 ± 4.0	14.3 ± 3.6
			185.5 ± 4.0	350.8 ± 12.1	143.9 ± 26.9
			350.8 ± 12.1	532.0 ± 0.0	45.7 ± 1.9
NGC 4081	Type II+III	21.76 ± 0.09	0.0 ± 0.0	23.1 ± 5.3	8.3 ± 0.5
			23.1 ± 5.3	51.4 ± 3.2	6.6 ± 0.3
			51.4 ± 3.2	64.1 ± 0.0	15.9 ± 3.2
NGC 4111	Type II	24.32 ± 0.13	32.2 ± 0.0	100.6 ± 7.2	28.7 ± 1.6
			100.6 ± 7.2	167.2 ± 0.0	19.5 ± 0.6
NGC 4330	Type II+III+II	25.04 ± 0.04	15.1 ± 0.0	55.6 ± 1.0	53.5 ± 2.7
			55.6 ± 1.0	72.9 ± 0.9	11.8 ± 0.6
			72.9 ± 0.9	85.4 ± 1.6	$\infty \pm \infty$
			85.4 ± 1.6	172.9 ± 0.0	22.5 ± 0.4
NGC 4359	Type III	24.55 ± 0.10	0.0 ± 0.0	70.7 ± 9.6	17.0 ± 0.8
			70.7 ± 9.6	140.8 ± 0.0	25.8 ± 1.6
NGC 4437	Type II	25.88 ± 0.03	39.4 ± 0.0	208.8 ± 2.9	101.2 ± 1.7
			208.8 ± 2.9	401.9 ± 0.0	42.9 ± 0.5
NGC 4565	Type II+II	25.53 ± 0.24	98.4 ± 0.0	211.9 ± 21.6	133.7 ± 28.8
			211.9 ± 21.6	436.3 ± 5.7	75.5 ± 2.5
			436.3 ± 5.7	500.0 ± 0.0	27.7 ± 1.5
NGC 4607	Type II+III	23.16 ± 0.18	17.6 ± 0.0	39.0 ± 2.7	22.1 ± 2.8
			39.0 ± 2.7	60.7 ± 2.9	8.5 ± 0.9
			60.7 ± 2.9	135.9 ± 0.0	20.4 ± 0.7
NGC 4747	Type I	24.22 ± 0.07	7.6 ± 0.0	126.7 ± 0.0	19.4 ± 0.4
NGC 5084	Type III	23.82 ± 0.17	37.5 ± 0.0	146.4 ± 8.6	30.4 ± 1.8
			146.4 ± 8.6	414.7 ± 0.0	72.4 ± 2.3
NGC 5470	Type II	23.77 ± 0.27	15.1 ± 0.0	60.0 ± 3.9	24.3 ± 4.4
			60.0 ± 3.9	98.4 ± 0.0	8.8 ± 0.5
NGC 5529	Type II+III+II	24.39 ± 0.12	13.9 ± 0.0	95.8 ± 5.7	35.3 ± 2.5
			95.8 ± 5.7	119.3 ± 7.0	10.8 ± 3.3
			119.3 ± 7.0	194.8 ± 28.1	40.2 ± 6.3
			194.8 ± 28.1	204.5 ± 0.0	19.5 ± 16.7
NGC 5981	Type II	23.17 ± 0.13	20.2 ± 0.0	52.0 ± 2.1	20.7 ± 1.4
			52.0 ± 2.1	102.1 ± 0.0	11.5 ± 0.2
NGC 6010	Type II	23.78 ± 0.40	20.2 ± 0.0	40.2 ± 3.9	22.9 ± 8.1
			40.2 ± 3.9	87.9 ± 0.0	10.7 ± 0.2

Table 4
(Continued)

ID	Type	I_0 (mag as^{-3})	r_i ($''$)	r_o ($''$)	h ($''$)
NGC 7347	Type II	22.79 ± 0.00	13.9 ± 0.0	41.3 ± 0.0	11.0 ± 0.0
			41.3 ± 0.0	59.0 ± 0.0	4.9 ± 0.0
PGC 013646	Type II	24.73 ± 0.00	13.9 ± 0.0	57.4 ± 0.0	84.4 ± 0.1
			57.4 ± 0.0	122.3 ± 0.0	11.5 ± 0.0
PGC 028308	Type II	22.04 ± 0.09	4.9 ± 0.0	59.9 ± 8.5	8.9 ± 0.2
			59.9 ± 8.5	64.1 ± 0.0	4.9 ± 3.0
PGC 030591	Type I	22.25 ± 0.21	16.3 ± 0.0	61.5 ± 0.0	7.6 ± 0.3
PGC 032548	Type I	24.10 ± 0.08	5.7 ± 0.0	59.0 ± 0.0	9.2 ± 0.2
PGC 052809	Type II	24.16 ± 0.19	11.7 ± 0.0	70.0 ± 5.4	28.4 ± 3.4
			70.0 ± 5.4	126.7 ± 0.0	13.2 ± 0.6
UGC 00903	Type II+III	21.14 ± 0.19	4.9 ± 0.0	18.4 ± 1.7	12.7 ± 2.8
			18.4 ± 1.7	22.7 ± 1.8	3.1 ± 1.2
			22.7 ± 1.8	64.1 ± 0.0	8.0 ± 0.1
UGC 01970	Type III+II	22.91 ± 0.10	5.7 ± 0.0	16.5 ± 1.1	6.1 ± 0.2
			16.5 ± 1.1	47.7 ± 3.4	17.8 ± 1.4
			47.7 ± 3.4	78.3 ± 0.0	9.9 ± 0.5
UGC 05347	Type II	24.70 ± 0.33	6.7 ± 0.0	30.1 ± 4.2	14.7 ± 4.2
			30.1 ± 4.2	49.6 ± 0.0	6.0 ± 0.5
UGC 05689	Type II	23.15 ± 0.33	4.0 ± 0.0	22.2 ± 9.9	9.6 ± 2.6
			22.2 ± 9.9	43.3 ± 0.0	6.8 ± 0.6
UGC 05958	Type I	23.17 ± 0.12	7.6 ± 0.0	59.0 ± 0.0	8.5 ± 0.2
UGC 06526	Type III	22.81 ± 0.11	6.7 ± 0.0	40.4 ± 3.2	8.3 ± 0.3
			40.4 ± 3.2	87.9 ± 0.0	15.2 ± 1.0
UGC 07086	Type II+III	22.58 ± 0.09	0.0 ± 0.0	31.7 ± 2.2	12.8 ± 0.9
			31.7 ± 2.2	36.7 ± 2.2	5.2 ± 1.6
			36.7 ± 2.2	87.9 ± 0.0	13.2 ± 0.4
UGC 08737	Type II+III	22.61 ± 0.21	15.1 ± 0.0	32.4 ± 3.2	19.3 ± 3.1
			32.4 ± 3.2	95.8 ± 5.0	9.3 ± 0.3
			95.8 ± 5.0	118.0 ± 0.0	56.9 ± 31.6
UGC 09448	Type I	22.94 ± 0.07	8.6 ± 0.0	47.5 ± 0.0	8.4 ± 0.2
UGC 09665	Type II	22.95 ± 0.34	4.9 ± 0.0	13.7 ± 5.3	19.8 ± 13.1
			13.7 ± 5.3	64.1 ± 0.0	8.5 ± 0.3
UGC 10043	Type II	23.78 ± 0.19	18.8 ± 0.0	69.7 ± 4.4	15.5 ± 1.1
			69.7 ± 4.4	81.4 ± 0.0	6.6 ± 1.2
UGC 10288	Type II+III	24.27 ± 0.31	13.9 ± 0.0	55.7 ± 13.2	38.9 ± 12.7
			55.7 ± 13.2	105.5 ± 25.0	19.2 ± 3.4
			105.5 ± 25.0	197.8 ± 0.0	24.5 ± 1.2
UGC 10297	Type II+III	24.37 ± 0.12	0.0 ± 0.0	12.8 ± 2.3	18.6 ± 4.9
			12.8 ± 2.3	37.4 ± 3.4	7.8 ± 0.5
			37.4 ± 3.4	64.1 ± 0.0	13.2 ± 0.9
UGC 12518	Type II+III	23.09 ± 0.42	7.6 ± 0.0	27.2 ± 4.9	14.2 ± 5.7
			27.2 ± 4.9	51.3 ± 5.5	5.9 ± 0.7
			51.3 ± 5.5	72.4 ± 0.0	11.6 ± 1.9
UGC 12692	Type III	21.63 ± 0.21	7.6 ± 0.0	32.5 ± 5.2	5.2 ± 0.3
			32.5 ± 5.2	54.2 ± 0.0	9.0 ± 2.0
UGC 12857	Type I	22.99 ± 0.12	9.6 ± 0.0	69.5 ± 0.0	9.7 ± 0.3

Notes. r_i and r_o stand for the inner and the outer limit of each fitted section and h corresponds to the scale length of that section. The lower limit of the innermost section and the upper limit of the outermost section have no error bar because they have been set manually.

In the literature, for a galaxy with a single disk in equilibrium, disks are ensured to have a roughly constant scale height by setting them to be $z_t = \sigma_t^2/(\pi G S)$ = constant at all radii (see, e.g., van der Kruit & Searle 1981a). The ratio of the squared velocity dispersion and the surface mass density does not directly control the disk scale height in a galaxy with two disks, however, setting it to be constant ($\sigma_i^2/(\pi G S)$ = constant) still ensures scale heights not to vary too much with r in the absence of perturbing effects such as those of a dark matter halo. In this context, S is the total face-on column mass density,

Table 5
Results of the Fits to Horizontal Luminosity Profiles for the Thick Disk

ID	Type	I_0 (mag as^{-3})	r_i ($''$)	r_o ($''$)	h ($''$)
ESO 157-049	Type II	27.08 ± 0.19	1.5 ± 0.0	25.1 ± 6.9	25.7 ± 8.8
			25.1 ± 6.9	72.4 ± 0.0	13.7 ± 0.7
ESO 240-011	Type I	28.37 ± 0.08	0.0 ± 0.0	131.3 ± 0.0	33.1 ± 1.1
ESO 292-014	Type II	28.99 ± 0.15	6.7 ± 0.0	58.7 ± 6.0	61.8 ± 11.8
			58.7 ± 6.0	84.6 ± 0.0	18.8 ± 2.2
ESO 346-001	Type II	27.33 ± 0.21	5.7 ± 0.0	31.3 ± 10.8	18.0 ± 3.7
			31.3 ± 10.8	56.6 ± 0.0	12.1 ± 1.3
ESO 440-027	Type I	27.95 ± 0.00	9.6 ± 0.0	172.9 ± 0.0	37.8 ± 0.0
ESO 443-021	Type I	28.00 ± 0.12	11.7 ± 0.0	64.1 ± 0.0	19.4 ± 0.9
ESO 466-014	Type I	26.93 ± 0.15	7.6 ± 0.0	41.3 ± 0.0	11.4 ± 0.6
ESO 469-015	Type I	27.21 ± 0.16	4.9 ± 0.0	54.2 ± 0.0	12.9 ± 0.7
ESO 533-004	Type II	27.73 ± 0.22	7.6 ± 0.0	38.7 ± 7.0	34.7 ± 10.3
			38.7 ± 7.0	84.6 ± 0.0	17.1 ± 0.8
ESO 544-027	Type II	27.07 ± 0.28	2.3 ± 0.0	10.7 ± 7.5	24.8 ± 20.3
			10.7 ± 7.5	45.3 ± 0.0	11.4 ± 0.7
IC 0217	Type II	28.73 ± 0.11	4.9 ± 0.0	36.1 ± 3.7	81.2 ± 26.3
			36.1 ± 3.7	91.3 ± 0.0	22.5 ± 0.8
IC 0610	Type I	26.66 ± 0.00	4.9 ± 0.0	69.5 ± 0.0	16.2 ± 0.0
IC 1197	Type II	27.49 ± 0.21	17.6 ± 0.0	40.8 ± 11.7	29.2 ± 5.8
			40.8 ± 11.7	94.8 ± 0.0	19.6 ± 1.1
IC 1553	Type I	27.55 ± 0.24	16.3 ± 0.0	49.6 ± 0.0	14.0 ± 1.2
IC 1711	Type I	28.37 ± 0.17	22.9 ± 0.0	87.9 ± 0.0	24.8 ± 1.5
IC 1913	Type I	29.60 ± 0.13	0.0 ± 0.0	69.5 ± 0.0	34.1 ± 2.7
IC 2058	Type II	28.31 ± 0.15	9.6 ± 0.0	72.7 ± 12.0	42.8 ± 6.4
			72.7 ± 12.0	113.8 ± 0.0	24.3 ± 2.2
IC 2135	Type II	27.49 ± 0.07	0.8 ± 0.0	78.8 ± 4.4	45.0 ± 3.3
			78.8 ± 4.4	122.3 ± 0.0	19.5 ± 0.9
IC 5176	Type III	27.12 ± 0.26	24.3 ± 0.0	75.9 ± 12.1	23.2 ± 3.0
			75.9 ± 12.1	150.9 ± 0.0	41.3 ± 3.0
NGC 0489	Type I	27.02 ± 0.09	0.0 ± 0.0	49.6 ± 0.0	12.4 ± 0.4
NGC 0522	Type II	27.94 ± 0.24	12.8 ± 0.0	63.2 ± 7.4	40.9 ± 10.8
			63.2 ± 7.4	98.4 ± 0.0	16.0 ± 1.5
NGC 0678	Type II	32.14 ± 0.51	39.4 ± 0.0	107.0 ± 7.4	−80.4 ± 44.8
			107.0 ± 7.4	145.8 ± 0.0	27.4 ± 4.1
NGC 1032	Type I	29.50 ± 0.06	0.0 ± 0.0	172.9 ± 0.0	53.7 ± 1.5
NGC 1163	Type I	27.73 ± 0.18	9.6 ± 0.0	87.9 ± 0.0	21.1 ± 1.3
NGC 1422	Type I	28.46 ± 0.06	4.0 ± 0.0	109.8 ± 0.0	33.1 ± 0.8
NGC 1495	Type I	28.10 ± 0.08	9.6 ± 0.0	98.4 ± 0.0	30.7 ± 1.0
NGC 1596	Type I	29.62 ± 0.07	0.0 ± 0.0	241.0 ± 0.0	72.9 ± 2.3
NGC 2732	Type II	27.04 ± 0.08	0.0 ± 0.0	52.9 ± 4.3	22.8 ± 1.4
			52.9 ± 4.3	78.3 ± 0.0	12.6 ± 0.8
NGC 3098	Type I	26.99 ± 0.08	4.9 ± 0.0	87.9 ± 0.0	19.0 ± 0.5
NGC 3279	Type II	28.04 ± 0.12	4.9 ± 0.0	52.1 ± 8.4	38.6 ± 5.7
			52.1 ± 8.4	84.6 ± 0.0	21.8 ± 1.6
NGC 3454	Type II	29.61 ± 0.07	0.0 ± 0.0	36.3 ± 3.3	$\infty \pm \infty$
			36.3 ± 3.3	91.3 ± 0.0	25.0 ± 1.3
NGC 3501	Type I	28.26 ± 0.07	18.8 ± 0.0	126.7 ± 0.0	34.3 ± 0.8
NGC 3592	Type II	28.24 ± 0.18	11.7 ± 0.0	36.3 ± 8.0	35.6 ± 8.5
			36.3 ± 8.0	72.4 ± 0.0	19.0 ± 1.4
NGC 3600	Type III	27.58 ± 0.11	4.9 ± 0.0	74.6 ± 9.1	17.7 ± 1.0
			74.6 ± 9.1	118.0 ± 0.0	120.6 ± 51.8

Table 5
(Continued)

ID	Type	I_0 (mag as^{-3})	r_i ($''$)	r_o ($''$)	h ($''$)
NGC 3628	Type II	28.95 ± 0.16	69.5 ± 0.0	383.5 ± 18.1	219.3 ± 34.2
			383.5 ± 18.1	532.0 ± 0.0	58.3 ± 4.9
NGC 4081	Type I	26.77 ± 0.06	9.6 ± 0.0	64.1 ± 0.0	16.9 ± 0.3
NGC 4111	Type I	29.00 ± 0.10	13.9 ± 0.0	145.8 ± 0.0	45.2 ± 2.0
NGC 4330	Type II	29.09 ± 0.06	0.0 ± 0.0	115.4 ± 5.4	87.5 ± 7.3
			115.4 ± 5.4	167.2 ± 0.0	30.5 ± 1.7
NGC 4359	Type I	28.70 ± 0.03	13.9 ± 0.0	135.9 ± 0.0	36.7 ± 0.3
NGC 4437	Type II	30.66 ± 0.00	39.4 ± 0.0	297.9 ± 0.0	151.5 ± 0.0
			297.9 ± 0.0	332.5 ± 0.0	73.1 ± 0.0
NGC 4565	Type I	30.13 ± 0.04	78.3 ± 0.0	469.9 ± 0.0	130.4 ± 1.8
NGC 4607	Type I	27.29 ± 0.03	1.5 ± 0.0	135.9 ± 0.0	28.9 ± 0.3
NGC 4747	Type I	27.93 ± 0.06	7.6 ± 0.0	126.7 ± 0.0	37.4 ± 0.9
NGC 5084	Type III	28.10 ± 0.13	37.5 ± 0.0	217.6 ± 19.3	58.8 ± 3.8
			217.6 ± 19.3	427.9 ± 0.0	150.0 ± 13.9
NGC 5470	Type II	28.07 ± 0.11	4.0 ± 0.0	71.8 ± 5.4	35.6 ± 3.4
			71.8 ± 5.4	87.9 ± 0.0	12.4 ± 2.2
NGC 5529	Type III+II	28.20 ± 0.01	27.3 ± 0.0	132.1 ± 0.5	36.6 ± 0.1
			132.1 ± 0.5	200.0 ± 0.9	$\infty \pm \infty$
			200.0 ± 0.9	204.5 ± 0.0	25.5 ± 1.1
NGC 5981	Type I	28.15 ± 0.06	6.7 ± 0.0	102.1 ± 0.0	29.6 ± 0.7
NGC 6010	Type I	28.20 ± 0.04	0.0 ± 0.0	91.3 ± 0.0	25.2 ± 0.5
NGC 7347	Type I	27.93 ± 0.15	6.7 ± 0.0	54.2 ± 0.0	17.6 ± 1.1
PGC 013646	Type I	28.25 ± 0.06	7.6 ± 0.0	113.8 ± 0.0	31.1 ± 0.7
PGC 028308	Type I	28.00 ± 0.21	13.9 ± 0.0	56.6 ± 0.0	22.3 ± 2.1
PGC 030591	Type I	27.59 ± 0.20	9.6 ± 0.0	45.3 ± 0.0	13.6 ± 1.0
PGC 032548	Type I	28.82 ± 0.29	0.0 ± 0.0	43.3 ± 0.0	17.5 ± 2.8
PGC 052809	Type II	28.01 ± 0.10	2.3 ± 0.0	82.8 ± 3.5	56.3 ± 6.6
			82.8 ± 3.5	122.3 ± 0.0	15.5 ± 0.9
UGC 00903	Type I	26.53 ± 0.07	1.5 ± 0.0	59.0 ± 0.0	14.7 ± 0.4
UGC 01970	Type I	29.09 ± 0.10	13.9 ± 0.0	75.3 ± 0.0	28.5 ± 1.3
UGC 05347	Type I	28.67 ± 0.23	9.6 ± 0.0	35.7 ± 0.0	15.8 ± 1.8
UGC 05689	Type II	27.66 ± 0.08	2.3 ± 0.0	17.3 ± 3.4	17.3 ± 1.6
			17.3 ± 3.4	43.3 ± 0.0	11.4 ± 0.5
UGC 05958	Type I	27.70 ± 0.18	7.6 ± 0.0	64.1 ± 0.0	17.4 ± 1.2
UGC 06526	Type I	28.23 ± 0.08	0.0 ± 0.0	87.9 ± 0.0	25.2 ± 0.9
UGC 07086	Type I	26.98 ± 0.11	4.9 ± 0.0	87.9 ± 0.0	18.8 ± 0.7
UGC 08737	Type I	27.05 ± 0.09	15.1 ± 0.0	122.3 ± 0.0	24.5 ± 0.7
UGC 09448	Type I	26.89 ± 0.25	8.6 ± 0.0	37.5 ± 0.0	10.8 ± 1.0
UGC 09665	Type I	27.66 ± 0.09	4.0 ± 0.0	59.0 ± 0.0	17.7 ± 0.7
UGC 10043	Type I	28.42 ± 0.25	22.9 ± 0.0	78.3 ± 0.0	25.8 ± 2.6
UGC 10288	Type I	27.88 ± 0.03	18.8 ± 0.0	156.1 ± 0.0	35.3 ± 0.3
UGC 10297	Type I	28.37 ± 0.24	6.7 ± 0.0	39.4 ± 0.0	14.6 ± 1.7
UGC 12518	Type I	27.32 ± 0.10	2.3 ± 0.0	72.4 ± 0.0	17.4 ± 0.6
UGC 12692	Type I	27.57 ± 0.01	5.7 ± 0.0	49.6 ± 0.0	13.8 ± 0.0
UGC 12857	Type I	28.35 ± 0.20	9.6 ± 0.0	49.6 ± 0.0	18.0 ± 1.6

Notes. r_i and r_o stand for the inner and the outer limit of each fitted section and h corresponds to the scale length of that section. The lower limit of the innermost section and the upper limit of the outermost section have no error bar because they have been set manually.

also accounting for gas. Thus, we implemented this condition in our models. The models were computed for $r < 2.0r_{25}$, but the exact radius at which the computation ends is not important.

Additionally, the computed grid of models has the following properties, which cover the range of possibilities found in our fits to observed galaxies.

1. Two very different star formation histories for the thick disk: $\Upsilon_T/\Upsilon_t = 1.2$ and $\Upsilon_T/\Upsilon_t = 2.4$.
2. Three face-on column mass density ratios at $r = 0$ yielding ρ_{T0}/ρ_{t0} values compatible with what is observed in our vertical fits: $S_T/S_t = 1/15$, $S_T/S_t = 1/10$, and $S_T/S_t = 1/5$.
3. Four truncation radii for the thin disk: $r_{t1,2} = 0.3r_{25}$, $r_{t1,2} = 0.6r_{25}$, $r_{t1,2} = 0.9r_{25}$, and $r_{t1,2} = \infty$. We have not considered truncations in thick disks. As shown in later sections, they are usually found to happen at very low surface brightness levels, and thus not likely to affect much the fits.
4. Two vertical velocity dispersion ratios typical of what we find in our vertical fits: $\sigma_T/\sigma_t = 2.0$ and $\sigma_T/\sigma_t = 2.3$.
5. Two thick disk scale lengths typical of what we find in our vertical fits: $h_T = 0.3r_{25}$ and $h_T = 0.6r_{25}$.
6. Models with no dark matter halo and models with a pseudo-isothermal dark matter halo (van Albada et al. 1985) with a core radius $r_c = 3.52$ kpc and a maximum circular velocity $v_c = 110\,\mathrm{km\,s^{-1}}$. This core radius is slightly larger than the inner thin disk scale length $r_c = 1.28h_{t1}$. The selected circular velocity corresponds to the median velocity in our 70 galaxy sample. The formalism used for describing the dark matter halo (dK_{DM}/dz) can be found in Narayan & Jog (2002) and CO11b.
7. Two gas distributions: one case with no gas at all and one case in which the face-on gas column mass density is constant with radius and equal to $S_g = 12\,M_\odot\,\mathrm{pc^{-2}}$ and with a vertical velocity dispersion $\sigma_g = 1/3\sigma_t$. This second gas distribution is qualitatively similar to that observed in many galaxies in the Bigiel et al. (2008) sample, but has a higher surface mass density in order to study what extreme gas mass distributions may do to our fits.
8. Six galaxy inclinations: $i = 90°, i = 89°, i = 88°, i = 87°$, $i = 86°$, and $i = 85°$.

Model fits were produced, like in our observed galaxies, for bins $0.2r_{25} < |R| < 0.5r_{25}$ and $0.5r_{25} < |R| < 0.8r_{25}$, with six different dynamical ranges which cover those found in observed galaxy fits: $\Delta m = 4.5$, $\Delta m = 5.0$, $\Delta m = 5.5$, $\Delta m = 6.0$, $\Delta m = 6.5$, and $\Delta m = 7.0$. In all of the cases, we fitted the models with the function of two stellar disks and a gas disk, the latter having 20% of the column mass density of the thin disk.

The total number of fits was 27,648. We excluded from our analysis 162 wrong fits ($\chi^2 > 0.01\ \left(\mathrm{mag\,arcsec^{-2}}\right)^2$), 10,562 fits compatible with a single-disk distribution according to the criterion presented in Section 3.5, and 1537 fits for which $(\Sigma_T/\Sigma_t)_f > 2.1$ because such massive thick disks have not been found in our observed galaxies. The remaining number of fits is 15,387.

4.2. Effect of Loosening Our Assumptions into the Fitted z_s

4.2.1. Reliability of the Fitted z_s

Because the goal of this paper is to study thin and thick disk horizontal luminosity profiles, it is important to know whether most light above a fitted z_s is emitted by the thick disk. This issue is addressed in Figure 4, in which it is shown that the fraction of light above the fitted z_s peaks around $f_T = 0.9$, with $f_T > 0.8$ for over 99% of the fits. Only one valid model has $f_T < 0.7$. It thus seems reasonable to say that the fitted z_s is good enough to define the limit of the region dominated by the thick disk.

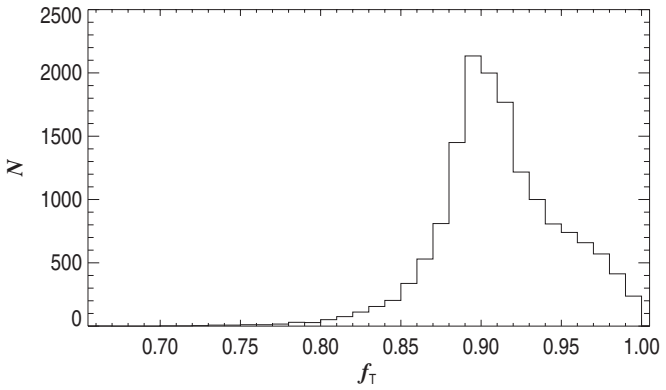

Figure 4. Histogram representing the fraction of light emitted by the thick disk for heights above the fitted z_s (f_T) in the set of 15,387 model galaxies considered for study (see the text).

4.2.2. z_s Variations with Radius

When selecting "valid" vertical profile fits, we assumed that z_s should vary by less than a factor of 1.5 within the fitted vertical bins. Thanks to our modeling, we can test the stability of z_s with varying projected radii. For every modeled galaxy, we compared z_s in the $0.2r_{25} < |R| < 0.5r_{25}$ and $0.5r_{25} < |R| < 0.8r_{25}$ bins. We found that if each bin is fitted down to the same μ_1, then $z_s\,(0.2r_{25} < |R| < 0.5r_{25}) = 1.26 \pm 0.29 z_s\,(0.5r_{25} < |R| < 0.8r_{25})$. This is natural because in most of our models, the thick disk increases its relative mass fraction with increasing radii. In 8% of our models, $z_s\,(0.2r_{25} < |R| < 0.5r_{25}) > 1.5z_s\,(0.5r_{25} < |R| < 0.8r_{25})$, which would lead the outer bins to be ignored when calculating z_s.

4.3. Effect of Loosening Our Assumptions into the Fitted Σ_T/Σ_t

In order to check the effect of deviations from the assumptions in our vertical luminosity profile fits, we have produced the plots shown in Figure 5. In them, we compare the ratio of the fitted ratio of thick to thin column mass densities $(\Sigma_T/\Sigma_t)_f$ with that in the original model $(\Sigma_T/\Sigma_t)_m$. The displayed distributions have a significant scatter, which means that some galaxies may have their thick disk column mass density underestimated or overestimated. The purpose of this subsection is to clarify the origin of those biases. In each panel of Figure 5, we have divided the fits into several color-coded bins, for which we have produced a linear regression which crossed the origin. In the case $\Upsilon_T/\Upsilon_t = 1.2$, the more accurate the fitted $(\Sigma_T/\Sigma_t)_f$, the closer the slope of the linear regression, m, will be to one. Solid lines denote the position that points associated with a perfect fit should have in the plot. The data points tend to appear above the solid lines, which indicates that our thick disk relative masses tend to be overestimated by a factor of ~10% on average as described in the next subsections.

4.3.1. Σ_T/Σ_t Roughly Scales with Υ_T/Υ_t

The fitted edge-on thick to thin column mass ratios—$(\Sigma_T/\Sigma_t)_f$—are in general very similar, but slightly larger than

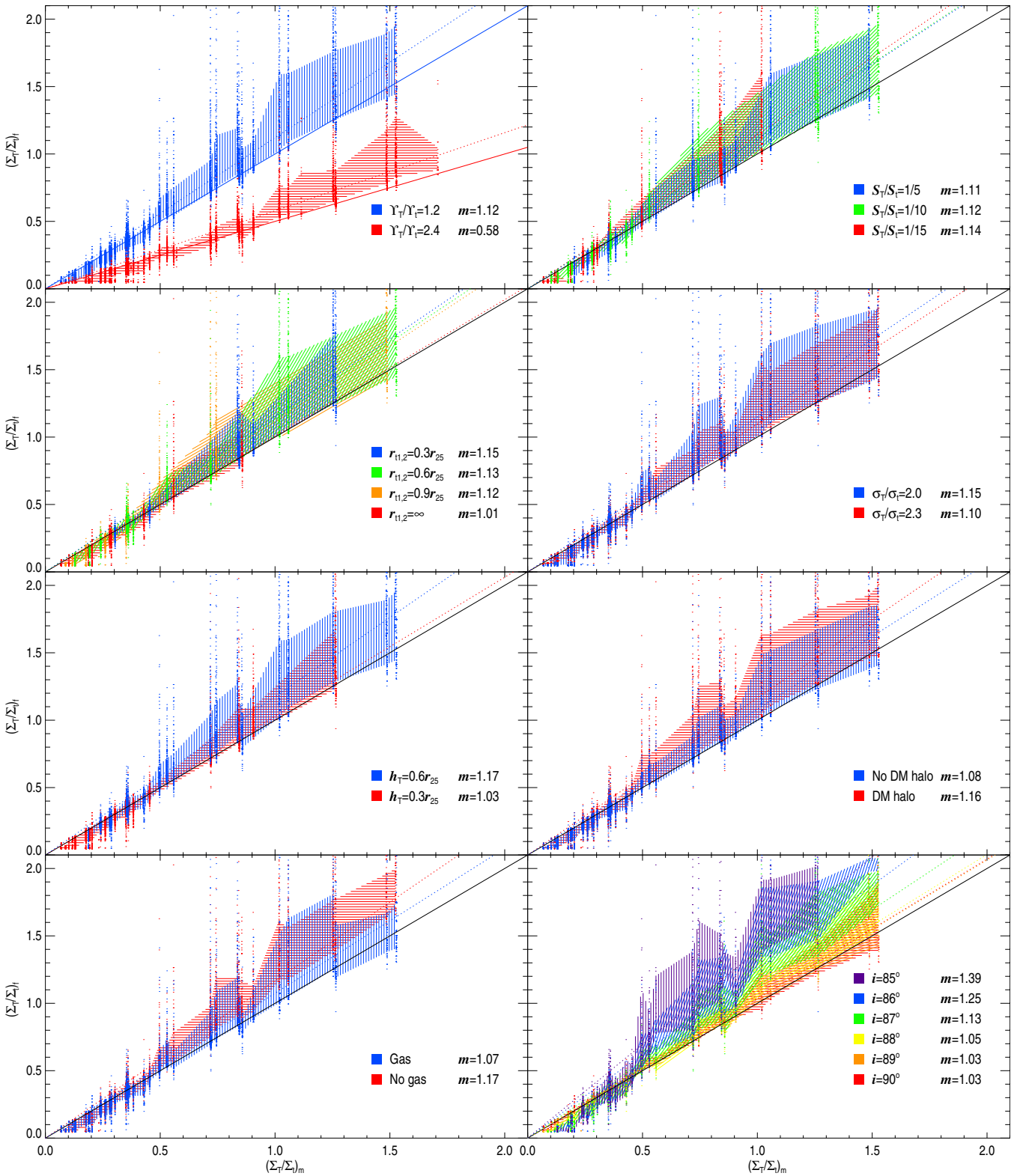

Figure 5. Comparison of the ratio of the thin and thick disk edge-on column mass densities in 15,387 galaxy models with varying properties (see the text for the selection criteria of the models). $(\Sigma_T/\Sigma_t)_f$ is the fitted edge-on column density ratio and $(\Sigma_T/\Sigma_t)_m$ the real ratio in the galaxy model. In the first panel, both $\Upsilon_T/\Upsilon_t = 1.2$ and $\Upsilon_T/\Upsilon_t = 2.4$ data are plotted. In the other panels, only the $\Upsilon_T/\Upsilon_t = 1.2$ data points are presented. Solid lines show $(\Sigma_T/\Sigma t)_f = (\Sigma_T/\Sigma t)_m$, except for the red line in the first panel, which shows $(\Sigma_T/\Sigma_t)_f = 0.5(\Sigma_T/\Sigma_t)_m$ as it would correspond if the light of the thin and the thick disk were correctly attributed by fits in the case $\Upsilon_T/\Upsilon_t = 2.4$. The dashed lines show linear regressions—forced to cross the origin—to models color-coded according to the properties described in the bottom-right corner of each panel. m denotes the slope of those fits. The hatched areas indicate the region which encloses 68.2% of the data points around the local $(\Sigma_T/\Sigma_t)_f$ median value.

(A color version of this figure is available in the online journal.)

that in the original model galaxy—$(\Sigma_T/\Sigma_t)_m$ when $\Upsilon_T/\Upsilon_t = 1.2$ ($m = 1.12$; top-left panel in Figure 5). When $\Upsilon_T/\Upsilon_t = 2.4$, the slope of the linear regression is $m = 0.58$, which is not very far from $m = 0.5$ and not far from being exactly half of the slope obtained for $\Upsilon_T/\Upsilon_t = 1.2$. This indicates that the fraction of light assigned to the thin and thick disks does not vary too much for a reasonable range of thick disk star formation histories and that Σ_T/Σ_t roughly scales with Υ_T/Υ_t as already pointed out in CO11b. Because of this close to linear behavior, it is easy to convert results obtained using a given Υ_T/Υ_t to another Υ_T/Υ_t. As a consequence, we will continue our analysis focusing on the $\Upsilon_T/\Upsilon_t = 1.2$ case.

4.3.2. Biases of the Fitted Σ_T/Σ_t

According to the linear fits made in Figure 5, the three main reasons for our fitted Σ_T/Σ_t to be overestimated are as follows.

1. *Inclination angles far from edge-on.* Galaxies with $i < 87°$ have their Σ_T/Σ_t overestimated on average by over 25%. However, our selection criteria should prevent many of these galaxies from being included in our sample.
2. *The thick disk scale length being significantly longer than the thin disk scale length.* if both scale lengths are similar, then the slope of the linear regression between the modeled and the fitted Σ_T/Σ_t is $m \sim 1$.
3. *The thin disk being truncated.* The smaller the truncation radius, the larger the risk of Σ_T/Σ_t being overestimated.

Other parameters that, to a lesser extent, contribute to overestimate the fitted Σ_T/Σ_t are as follows.

1. *A gas-depleted disk being fitted with a function including a significant gaseous disk.* This justifies fitting the vertical profiles of early-type galaxies with functions that do not include a gas disk.
2. *The disk being submaximal.*
3. *Low σ_T/σ_t values.*

Additionally, we noticed that in galaxies with the most dominant-fitted thick disks, the relative thick to thin disk masses are more easily overestimated. In Figure 5, data points appearing in the left side of a panel have a lower chance of being found above the $(\Sigma_T/\Sigma_t)_f = (\Sigma_T/\Sigma_t)_m$ line than those in the right side of the panel. This is also seen in the data presented in Table 6. Yoachim & Dalcanton (2006) and CO11b describe how the ratio of the stellar mass of the thick and the thin disk, M_T/M_t, decreases with increasing galaxy mass. One could interpret that the slope of this relationship has been overestimated because of the overestimate of thick disk masses in thick disk dominated galaxies. However, this effect is likely to be compensated for by the fact that Υ_T/Υ_t is probably larger in smaller galaxies, whose thin disks host in the local universe a larger relative star formation, which lowers Υ_t. The exact quantification of Υ_T/Υ_t is under study and will be published in a follow-up paper (S. Comerón et al. 2013, in preparation).

As a conclusion, in most of the cases, the overestimation of the thick disk is relatively small (generally less than a 20%). This could be compensated for by the fact that, among reasonable star formation histories for thin and thick disks, we have selected a mass-to-light ratio that yields the smaller thick disk relative mass ($\Upsilon_T/\Upsilon_t = 1.2$).

Table 6
Σ_T/Σ_t Overestimate as a Function of Σ_T/Σ_t Values in Models with $\Upsilon_T/\Upsilon_t = 1.2$

As a Function of the Fitted Column Mass Ratio	
$(\Sigma_T/\Sigma_t)_f$	$(\Sigma_T/\Sigma_t)_f/(\Sigma_T/\Sigma_t)_m$ (Overestimation factor)
$0.0 < (\Sigma_T/\Sigma_t)_f \leqslant 0.5$	0.90 ± 0.20
$0.5 < (\Sigma_T/\Sigma_t)_f \leqslant 1.0$	1.10 ± 0.15
$1.0 < (\Sigma_T/\Sigma_t)_f \leqslant 1.5$	1.24 ± 0.27
$1.5 < (\Sigma_T/\Sigma_t)_f \leqslant 2.1$	1.44 ± 0.36
As a Function of the Model Column Mass Ratio	
$(\Sigma_T/\Sigma_t)_m$	$(\Sigma_T/\Sigma_t)_f/(\Sigma_T/\Sigma_t)_m$ (Overestimation factor)
$0.0 < (\Sigma_T/\Sigma_t)_m \leqslant 0.5$	0.93 ± 0.23
$0.5 < (\Sigma_T/\Sigma_t)_m \leqslant 1.0$	1.19 ± 0.30
$1.0 < (\Sigma_T/\Sigma_t)_m \leqslant 1.5$	1.36 ± 0.49
$1.5 < (\Sigma_T/\Sigma_t)_m \leqslant 2.1$	1.52 ± 0.69

Note. The format of the data is average $\pm 1\sigma$.

5. RESULTS

5.1. Thick Disk Relative Masses

Our sample is larger than in CO11b and the criteria used to select which vertical luminosity profiles are "good" should guarantee our fits to be of better quality than those obtained in CO11b. This is why we replotted Figure 13 of CO11b—that relating the relative thick disk stellar mass with the galaxy circular velocity—in Figure 6. We can see how, as seen in Yoachim & Dalcanton (2006) and CO11b, the relative thick disk stellar mass, M_T/M_t anticorrelates with the circular velocity, v_c. The range of relative disk masses, $0.2 < M_T/M_t < 2.0$, is also very similar to that found in previous works.

In CO11b, four galaxies were outliers with $v_c \sim 200\,\mathrm{km\,s^{-1}}$ and $M_T/M_t \gtrapprox 1$. Only one of these galaxies appears in our new plot. The reason is that two of these galaxies, ESO 079-003 and NGC 4013, have not been included in our final sample because they have extended envelopes and were excluded by the $\mu_1 < 24.5\,\mathrm{mag\,arcsec^{-2}}$ criterion. A third galaxy, ESO 443-042, has been dropped because of a too noisy luminosity profile due to the vicinity of a nearby bright star. The only one of these outliers remaining is NGC 3628, an interacting galaxy in the Leo Triplet which we visually identified to have an extended component which is faint enough to go through our sample selection criteria. If we were making our selection criteria more restrictive, then we would be excluding galaxies which do not have an extended component other than a thin and a thick disk, so we decided to keep NGC 3628 in the sample. The galaxy appearing at $v_c \sim 300\,\mathrm{km\,s^{-1}}$ with $M_T/M_t \sim 2$ is NGC 5084, and what we fitted as the thick disk could actually be a very extended bulge.

Another galaxy with $M_T/M_t > 1$ that is interacting but which does not fall outside the main trend is NGC 4747, which has been perturbed by NGC 4725 (Haynes 1979).

We found that M_T/M_t is roughly constant for $v_c > 120\,\mathrm{km\,s^{-1}}$, with values $0.2 < M_T/M_t < 0.7$. For this range of velocities, the mean value of the stellar disk mass ratio is $M_T/M_t = 0.48 \pm 0.03$ once the two outliers, NGC 3628 and NGC 5084, have been excluded. Below that circular speed, there is a sudden increase of the typical M_T/M_t. This $v_c = 120\,\mathrm{km\,s^{-1}}$

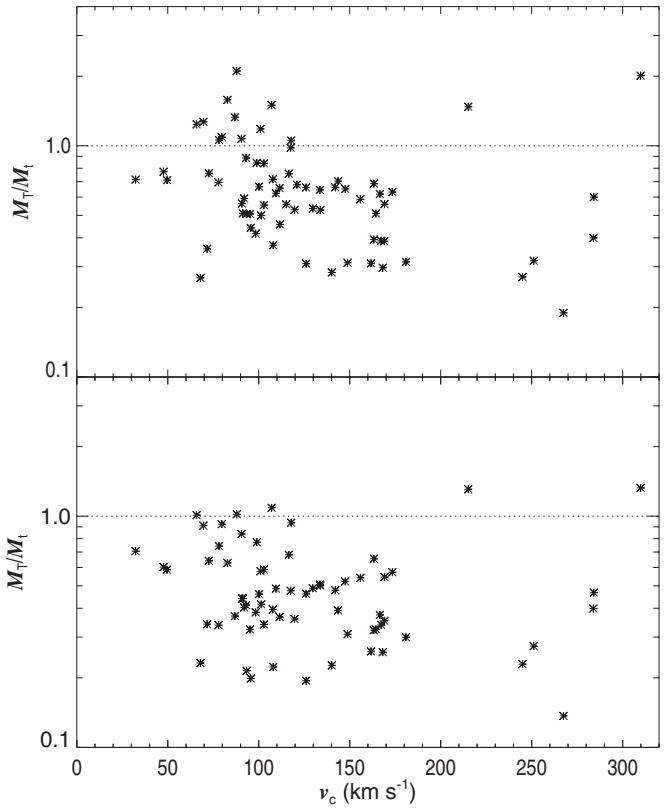

Figure 6. Ratio of the thick and the thin disk mass, M_T/M_t, as a function of the circular velocity, v_c. The top panel shows data points calculated using only the stellar thin disk and thick disks, and the bottom panel shows data points for which the gas disk has been included in the thin disk, as explained in Section 6.3.

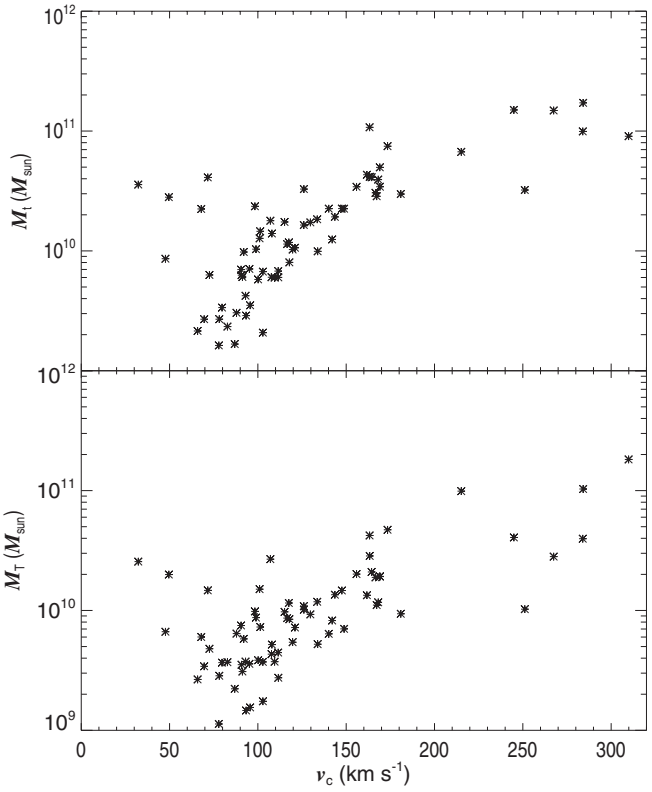

Figure 7. Absolute stellar masses of the thin (top panel) and the thick disk (bottom panel) as a function of circular velocity, v_c.

limit is the same below which Dalcanton et al. (2004) suggested that star formation becomes less efficient.

We calculated the thin and thick disk absolute masses by assuming $\Upsilon_t = 1$, $\Upsilon_T/\Upsilon_t = 1.2$, and that the 3.6 μm absolute magnitude of the Sun in the AB system is $M_\odot = 6.06$ mag (Oh et al. 2008). We found that both the thin and thick disk absolute masses increase with increasing v_c (Figure 7). However, the thin disk mass generally increases faster with v_c, which is the reason why M_T/M_t declines with increasing v_c. Also, M_T values have a larger scatter than the M_t ones.

5.2. The Breaks We Fit are Likely to be the Same as Those Observed in Face-on Galaxies

Truncations and antitruncations in edge-on galaxies have long been assumed to correspond to those seen in face-on galaxies (see, e.g., Kregel et al. 2002 and Pohlen et al. 2004b for review). However, before extracting any conclusions from our horizontal luminosity profile fits, it is important to assess whether our fitting approach is accurate enough when finding and describing breaks.

Truncation (Type II breaks) and antitruncation (Type III breaks) radii are known to have some correlation with galaxy properties such as brightness. We compared the distribution of our fitted break radius for the total luminosity profile as a function of galaxy absolute blue magnitude with those in the large face-on galaxy sample from Pohlen & Trujillo (2006), which consists of almost a hundred nearby galaxies ranging from Sb to Sdm galaxies (thus, unlike us, excluding early-type disk galaxies). The reason for using the total luminosity profiles is that Pohlen & Trujillo (2006) were not able to distinguish between thin and thick disk light due to the use of a sample of face-on galaxies.

Our galaxy absolute magnitudes were calculated by using HyperLEDA's internal dust extinction-corrected blue brightnesses and a distance modulus which makes use of the average redshift-independent distance measurements appearing in the NASA/IPAC Extragalactic Database (NED). For a few galaxies, no redshift-independent distance measurements were available and distances were determined from NED's Virgo Infall corrected radial velocities and a Hubble-Lemaître constant $H_0 = 73$ km s^{-1} Mpc^{-1}.

The results are presented in Figure 8 and we see how the distribution of truncation radii (top panel) and that of antitruncation radii (bottom panel) are very similar for the face-on galaxy sample (gray dots) and our edge-on sample (black dots). It is thus reasonable to think that our fitting method has properly captured break radii.

5.3. Classification of the Horizontal Luminosity Profile Fits

The fits to total, thin, and thick horizontal luminosity profiles were classified, using the Erwin et al. (2008) criteria, into Type I, Type II, Type III, or combinations of Type II and Type III profiles (composite luminosity profiles). For example, a galaxy with a Type II+III+II profile presents a truncation followed by an antitruncation and then a second truncation.

The individual classifications for each galaxy are presented in Tables 3, 4, and 5 for the total, the thin, and the thick disk, respectively. Pohlen & Trujillo (2006) and Erwin et al. (2008) use further subdivisions for Type II and Type III profiles, but those subdivisions require one to know properties, mostly related to the bar length, only easily measurable in face-on

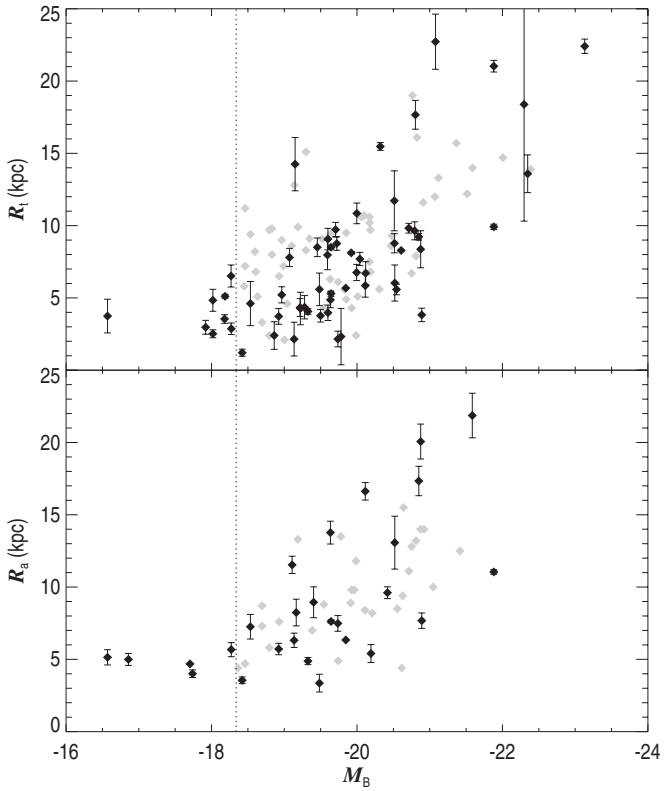

Figure 8. Top Panel: radii of the fitted truncations for the total disk as a function of the galaxy absolute blue magnitude. Bottom panel: radii of the fitted antitruncations for the total disk as a function of galaxy absolute blue magnitude. Black symbols correspond to the edge-on galaxies in this paper and gray symbols correspond to galaxies in Pohlen & Trujillo (2006). The vertical pointed lines represent the lower brightness limit of Pohlen & Trujillo's (2006) sample. Error bars represent 2σ fitting errors.

Table 7
Classification of the Horizontal Luminosity Profile Fits

Profile type	Total	Thin	Thick	PT06
Type I	7 (10%)	9 (13%)	45 (64%)	9 (11%)
Type II	32 (46%)	32 (46%)	21 (30%)	46 (54%)
Type III	9 (13%)	7 (10%)	3 (4%)	21 (25%)
Type II+II	3 (4%)	3 (4%)	0 (0%)	2 (2%)
Type II+III	15 (21%)	15 (21%)	0 (0%)	7 (8%)
Type III+II	1 (1%)	1 (1%)	1 (1%)	0 (0%)
Type II+III+II	3 (4%)	3 (4%)	0 (0%)	0 (0%)

Notes. Total, thin, and thick refer to total, thin, and thick horizontal luminosity profiles. PT06 refers to the galaxies classified in Pohlen & Trujillo (2006).

galaxies, so we have not been able to apply them to our sample. The result of the classification is summarized in Table 7.

Because the total luminosity profile is dominated by the light used to prepare the thin luminosity profile, the classifications for the total and the thin luminosity profiles are usually the same and the break radii are usually similar for both profiles.

Two of our total horizontal luminosity profiles—those made for NGC 3600 and NGC 5084—have an antitruncation which is an artifact caused by the presence of an extended bulge as is described in 15% of the galaxies in Maltby et al. (2012).

Because we can only detect breaks down to $\mu_{3.6\,\mu m}(\mathrm{AB}) = 25$–$26\,\mathrm{mag\,arcsec^{-2}}$ (see Section 5.4), our antitruncations are found at much brighter surface brightness than those which would be caused by a halo as described in Bakos & Trujillo (2012).

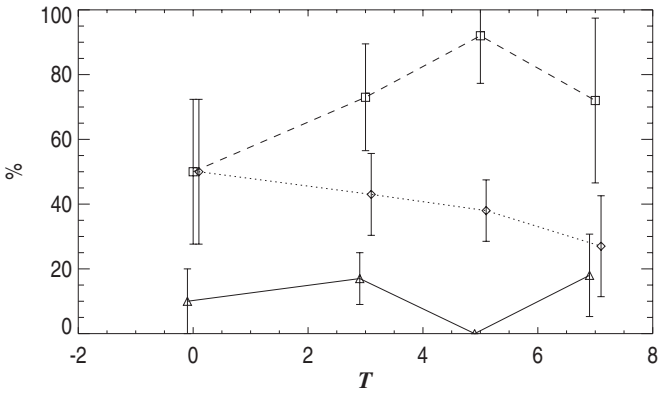

Figure 9. Fraction of galaxies having no breaks (triangle symbols and solid line), at least one truncation (square symbols and dashed line) and at least one antitruncation (diamond symbols and dotted line). The galaxies have been classified in four morphological type bins with $T \leqslant 2$, $2 < T \leqslant 4$, $4 < T \leqslant 6$, and $6 < T \leqslant 8$. The error bars are obtained by using Poisson binomial statistics.

When compared with the profile classification in Pohlen & Trujillo (2006), we find that our total luminosity profiles have similar percentages of Type I and Type II profiles. However, there is a significant difference in the percentage of Type III galaxies (25% for them compared to 13% for us) and the sum of Type II+III and Type II+III+II galaxies (8% for them compared to 25% for us). Since the sum of the fraction of Type III, Type II+III, and Type II+III+II galaxies is nearly the same for both samples, we checked whether we could be classifying some Type III galaxies as Type II+III or Type II+III+II. By looking at the luminosity profiles in Pohlen & Trujillo (2006), we found that 6 out of their 21 Type III galaxies have shoulders caused by star formation at the end of bars, inner rings, and/or prominent spiral arms which would have led us to classify those galaxies as Type II+III if seen in an edge-on view. These galaxies are NGC 1084, NGC 1087, NGC 1299, NGC 4668, UGC 09741, and UGC 10721. If the fraction of shoulders caused by these reasons was the same in our sample, then ~3–6 of our Type II+III (Type II+III+II) galaxies would be classified as Type III (Type III+II) by Pohlen & Trujillo (2006). Thus, some of the truncations we only see in the thin disk may actually be an artifact of components (bars, rings) with a low Υ. However, the number of misclassified galaxies could be smaller than the estimate we give, because these shoulders would get diluted due to line-of-sight integration and because the effect of star formation regions in rings and spiral arms should be less pronounced in the infrared (see, e.g., Buta et al. 2010).

As shown in Figure 9, we found that earlier-type galaxies tend to have less truncations than later-type galaxies in accordance with Figure 9 in Gutiérrez et al. (2011). The fraction of untruncated and antitruncated disks seems to remain roughly constant with type changes (especially if we consider that two of the antitruncations in the earlier-type bin are an artifact caused by bulges), but large error bars do not allow us to be sure. Again, these results seem to agree with those by Gutiérrez et al. (2011) which, for a larger sample of face-on galaxies, found a small decay in the frequency of untruncated disks when going to later types and a constant fraction of antitruncated disks.

5.4. Truncations in Thin and Thick Disks

We searched whether the truncations (Type II breaks) in thin and thick disks are qualitatively different. We first looked at how strong the truncations are by comparing the outer scale

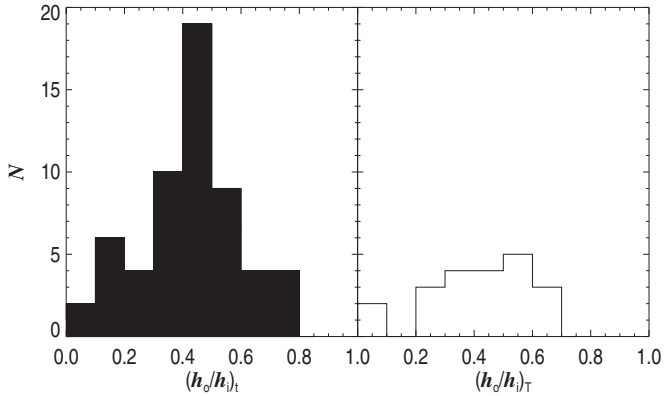

Figure 10. Ratio of the outer disk and the inner disk scale lengths in truncated profiles (Type II breaks) for the thin disk (left panel) and the thick disk (right panel). In the case of Type II+II and Type II+III+II profiles, both truncations have been considered.

length (h_o) and the inner scale length (h_i) in both thin and thick disks (Figure 10). We found that the h_o/h_i distributions are quite similar, except for a narrow peak in the thin disk scale length ratio ($(h_o/h_i)_t$). We also found that $(h_o/h_i)_t$ and $(h_o/h_i)_T$ are little correlated (linear Pearsons correlation coefficient $\rho \sim 0.3$).

When both the thin and the thick disk are truncated, the inner scale length of the thick disk is generally between one and two times that of the thin disk (Figure 11). The outer scale length of the thick disk is even less correlated with that of the outer thin disk than the inner thin and thick disk scale lengths. Because there is some contribution of thick disk light in the range of heights where we have measured thin disk properties, it is expected that the thin disk scale lengths, especially $(h_o)_t$, have been overestimated.

When plotting a histogram of the distribution of break radii, r_b, in units of the fitted inner disk scale lengths, we find that thick disks do generally truncate at a lower relative radius than thin disks (Figure 12), which is generally due to thick disks having a longer inner scale length.

A difference between truncations in thin and thick disks is their frequency. Fifty-four of our thin disks are truncated (77%), but only 22 of the thick disks are (31%). Thus, apparently, thin disks have more than double the frequency of truncations in thick disks. This could be due to an intrinsically lower fraction of truncations in thick disks or because we may not be able to detect them due to their low surface brightness. To test that we measured the surface brightness difference between the thin disk luminosity profile at $r = 0$ and that at the radius of the truncation, Δm_t. The thin disk surface brightness at the truncation radius was found directly from the luminosity profile, but that at $r = 0$ was found by using the fits of the truncated disk function integrated over the line of sight. The reason to do so was to avoid the bulge influence. We then searched for the surface brightness difference between the luminosity profile at $r = 0$ and the truncation detection threshold (Δm_T) in the thick disks. In Section 3.7, we explained that truncations were found visually before producing the actual fitting. Because of the subjective nature of this identification, the truncation detection threshold is unclear and we can only estimate it, making the Δm_T values rather uncertain. Based on our experience of visually classifying the breaks, we are confident that we detect truncations down to $\mu_{3.6\,\mu\mathrm{m}}(\mathrm{AB}) = 25$–$26\,\mathrm{mag\,arcsec^{-2}}$.

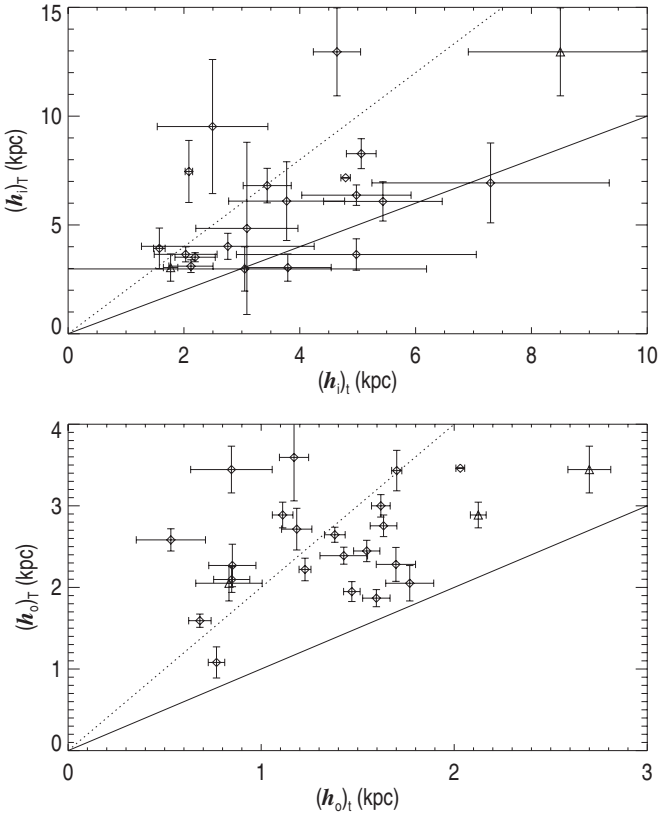

Figure 11. Scale lengths of inner thick disks as a function of their inner thin disks scale lengths (top panel) and scale lengths of outer thick disks as a function of their thin disk scale lengths (bottom panel) for galaxies with both thin and thick disk truncated. Solid lines trace a one-to-one relation between the thin and thick disk scale lengths and the dotted lines indicate thick disks with a scale length two times larger than that of the thin disk. Triangle symbols stand for the second truncation in Type II+II and Type II+III+II profiles. Error bars represent 2σ fitting errors.

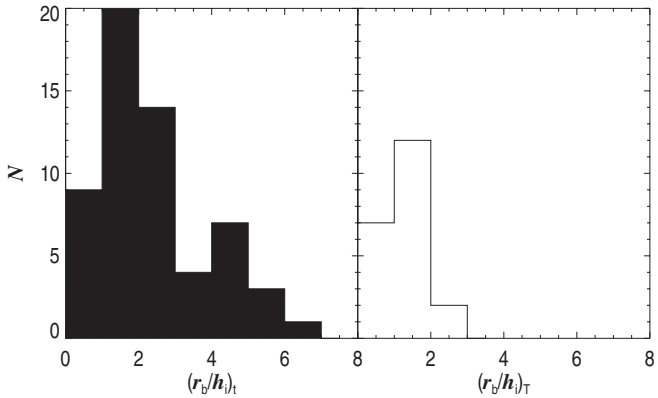

Figure 12. Ratio of the truncation break radius and the inner disk scale length for the thin disk (left panel) and the thick disk (right panel). In the case of Type II+II and Type II+III+II profiles, both truncations have been considered.

We compared the Δm_T for each thick disk to a random set of Δm_t measured from real thin disks, as explained before. If $\Delta m_t > \Delta m_T$, we considered that the particular thin disk truncation could not be detected on that particular thick disk. If our detection threshold was $\mu_{3.6\,\mu\mathrm{m}}(\mathrm{AB}) = 26\,\mathrm{mag\,arcsec^{-2}}$, then we would detect ∼60% of thick disk truncations. If our detection threshold was $\mu_{3.6\,\mu\mathrm{m}}(\mathrm{AB}) = 25\,\mathrm{mag\,arcsec^{-2}}$, then we would be detecting only ∼30% of the truncations. These numbers would be compatible with a similar frequency

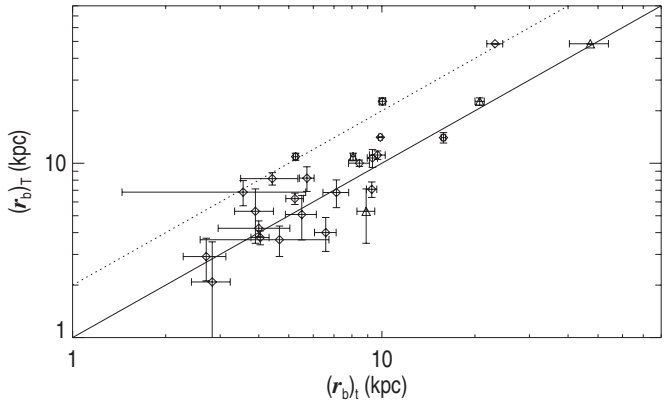

Figure 13. Truncation radii of thick disks as a function of truncation radii for thin disks. The solid line traces a one-to-one relation between the thin and the thick disk truncation radius and the dotted lines indicates thick disks with a truncation radius two times larger than that of the thin disk. Triangle symbols stand for the second truncation in Type II+II and Type II+III+II profiles. Error bars represent 2σ fitting errors.

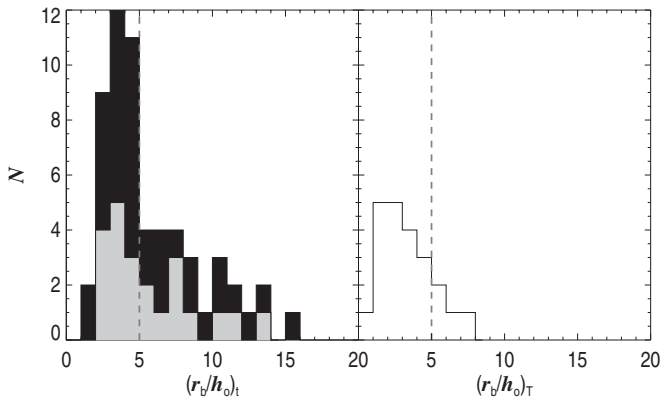

Figure 14. Ratio of the truncation break radius and the outer disk scale length for the thin disk (left panel) and the thick disk (right panel). In the case of Type II+II and Type II+III+II profiles, both truncations have been considered. The gray histogram indicates thin disk truncations which are associated with a thick disk truncation. The vertical dashed line shows the limit between inner truncations and outer truncations according to the definition in Martín-Navarro et al. (2012).

of truncations in thin and thick disks if thin and thick disk truncations were completely unrelated.

However, truncations in thin and thick disks are not completely uncorrelated because we found the truncation radius for the thin disk to be similar to that of the thick disk in most cases (Figure 13). In cases of galaxies with two thin disk truncations, the thick disk truncation has a radius similar to that of one of the thin disk truncations. It thus seems that thick disk truncations tend to be associated with a thin disk truncation. This is further discussed in Section 6.1.

Martín-Navarro et al. (2012) divided truncations into inner truncations and outer truncations. Inner truncations are those for which the ratio of the truncation radius and the outer disk scale length is smaller than 5, $r_b/h_o < 5$, and outer truncations are those for which this ratio is larger than 5, $r_b/h_o > 5$. We have checked in which category our truncations would fall (Figure 14). We found that our thin disks have both inner and outer truncations and that thick disks only have inner truncations or borderline cases. We have also checked how thin disk truncations associated with a thick disk truncation are distributed. Again, we found that they may be inner or outer.

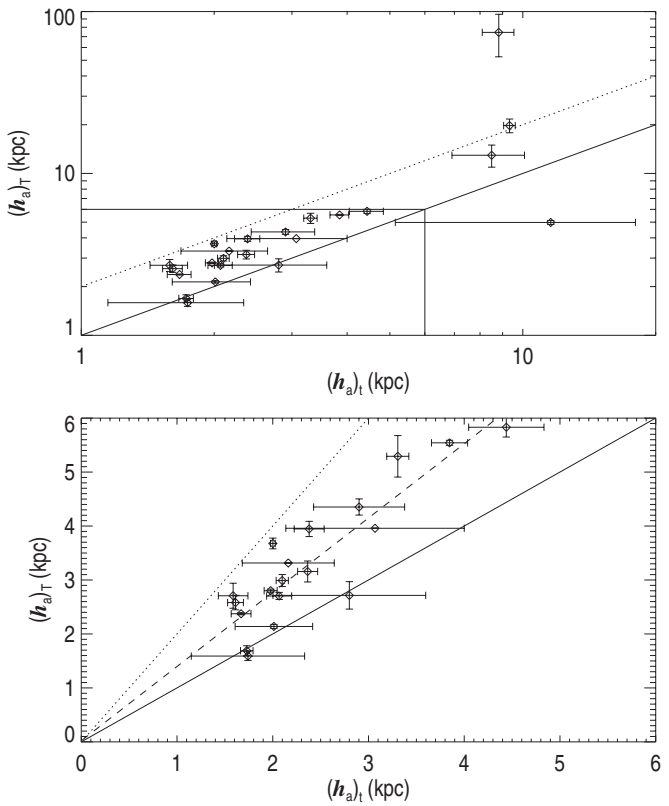

Figure 15. Thick disk scale length as a function of thin disk scale length for regions after a Type III break (antitruncation). In the bottom panel, the solid line represents a slope equal to one and the dotted line represents a slope equal to two; this factor of two ratio is indicated by the dotted line in the top panel too. The top panel shows the axis is a logarithmic scale and the bottom panel shows the range indicated by a box in the top panel with the axis displayed in a linear scale. The dashed line in the bottom panel represents the best linear fit for the galaxies displayed on it. Error bars represent 2σ fitting errors.

5.5. Antitruncations in Thin and Thick Disks

We define $(h_a)_t$ as the scale length of the thin disk in the section after an antitruncation (Type III break). We define $(h_a)_T$ as the scale length of the thick disk section that has the largest overlap in galactocentric projected radius with the thin disk section with scale length $(h_a)_t$.

We found that the fitted thin disk scale length after an antitruncation ($(h_a)_t$) and the fitted thick disk scale length at that radius ($(h_a)_T$) correlate quite well (Figure 15). If we consider the galaxies appearing in the lower panel, then the slope is roughly 1.4 and the Pearsons correlation coefficient is $\rho = 0.89$. The galaxies with $(h_a)_t > 6$ kpc have not been considered because they are outliers which highly affect the fit.

According to the data in Table 7, thick disks are very rarely found to antitruncate (6%) within the surface brightness limits we are studying. We individually checked the origin of the antitruncations in thick disks. That in NGC 5529 seems to be a genuine antitruncation, with the host galaxy having a significant warp. Additionally, NGC 5529 has at least four companion galaxies (Irwin et al. 2007) within 10 arcmin or 150 kpc in projection. The brighter of these satellite galaxies, MCG +06-31-085a, is around 4 mag fainter than the main galaxy and is connected to it by an H I bridge (Kregel et al. 2004), suggesting that the unusual thick disk antitruncation could be the consequence of an interaction. The antitruncations in NGC 3600 and NGC 5084 are related to the presence of

extended spherical bulges, whose light makes the scale height at radii smaller than the truncation radius steeper than it would be in the absence of a bulge. The case of IC 5176 seems to be rather similar, but the bulge is much flatter and thus not a classical bulge.

6. DISCUSSION

6.1. Truncations in Thick Disks Could be Linked to a Thin Disk Truncation

We found 60 truncations in thin disks (taking into account those truncated twice), for only 22 truncations in thick disks. In Section 5.4, we showed that if the difference in brightness between the disk center and the truncation radius was the same in thin and thick disks and we were considering truncations in both disks to be uncorrelated, we would be detecting only between ∼30% and ∼60% of truncations in thick disks.

However, most of the truncations we discovered in thick disks are found at a radius similar to that of the truncation of the thin disk. If thick disk truncations are systematically found at the same radius as their thin disk counterpart, then we should be detecting most of them. As a consequence of that, we can say that some thick disks in galaxies with a truncated thin disk are untruncated.

Further evidence of a truncation happening at the same radius for the thin and the thick disk appears in Radburn-Smith et al. (2012), who studied the truncation of the face-on galaxy NGC 7793 and found that if that galaxy had a significant thick disk—which is likely to be the case because of its low mass—then it has to truncate as the same radius as the thin disk.

This suggests two possible formation mechanisms for truncations: one creating truncations simultaneously both in the thin and the thick disk and one creating them only in the thin disk. A mechanism creating a truncation in both disks should be a dynamical one, because it is hard to conceive a star formation threshold at the same radius in the two disks at different times of galaxy evolution. This would make sense if we consider that Pohlen & Trujillo (2006) and Erwin et al. (2008) divide face-on truncations into four groups based on their morphology and radius compared to the bar length. The most frequent truncation types in their papers, and thus studied with most detail, are outer lindblad resonance (OLR) breaks, or Type II.o-OLR—thought to be close to bar Outer Lindbald Resonances—and classical truncations, or Type II.o-CT, which do not seem to be associated with the bar and the authors suggest they are related to star formation thresholds. Unfortunately, no galaxy property, except the ratio between the truncation radius and that of the bar, is clearly able to distinguish between those two kinds of truncations. To further complicate the picture, Muñoz-Mateos et al. (2012) suggest that some of the Type II.o-CT truncations could also be related to the OLR in the case of a bar+spiral rotation pattern coupling. Another possibility is that the same mechanism creates a truncation in one disk or in both depending on some galactic property which would not be related those we have studied in this paper (kinematics, spiral arms/bar properties,...).

We checked whether thin disk truncations associated with untruncated thick disks are qualitatively different than those associated with truncated thick disks, but we found no significant difference in galaxy morphological type, absolute magnitude, outer disk scale length compared to that of the inner disk ($(h_o/h_i)_t$), break radius in inner disk scale length units ($(r_b/h_i)_t$), or break radius in outer disk scale length units ($(r_b/h_o)_t$). This would be consistent with the Pohlen & Trujillo (2006) findings of two kinds of truncations—Type II.o-OLR and Type II.o-CT—which can only be differentiated by the bar position with respect to the truncation radius.

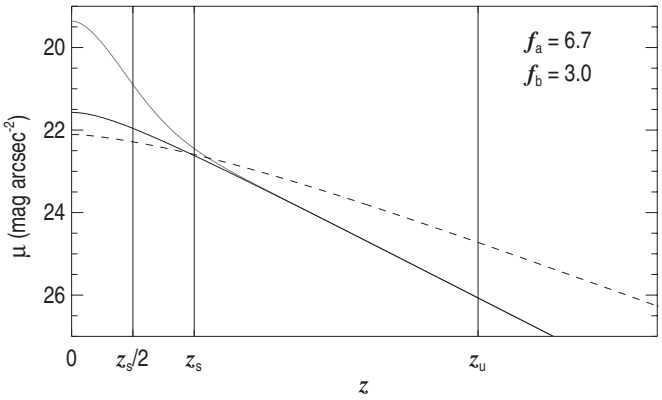

Figure 16. Vertical luminosity profile for an arbitrary galaxy in our sample (gray). The thick disk is shown in black and a thick disk with the same velocity dispersion and face-on surface brightness but after the removal of the thin disk is shown as a dashed line. The f_a and f_b values are displayed in the top-right corner.

If we consider that our classification of thin disk truncations into inner and outer types is valid, then an extra puzzle appears. Martín-Navarro et al. (2012) suggested that inner and outer breaks may have been formed in two different kind of processes. However, having thick disk truncations associated with both the inner and outer thin disk truncations shows that these two processes would both be able to build a thick disk truncation under the right circumstances. This variety of inner/outer truncations associated/non-associated with thick disk truncations indicates that the truncation mechanisms may be even more complex than expected.

6.2. Genuine Antitruncations are Rare

As seen in Section 5.5 and Figure 15, the scale length of the thin disk profile after an antitruncation break seems to correlate with the thick disk scale length at that projected radius. A visual inspection of the fits in Figure 17 shows that, in many cases, the shape of the luminosity profiles of Type III, Type II+III, and Type I+III+II thin disks after the antitruncation break radius, r_a, is very similar to that of the thick disk in the same projected radius range. It is therefore possible that it is not the thin disk itself which antitruncates, and that what we are actually seeing is that the thick disk dominates the light emission even in the range of heights $0 < z < 0.5z_s$ for $R > r_a$.

In order to test that possibility, we used the fits to vertical luminosity profiles and we calculated the mean flux per pixel emitted by the thick disk in the range $0 < z < 0.5z_s$ (height range for thin disk horizontal luminosity profiles) divided by the mean flux per pixel emitted at $z_s < z < 0.5z_u$ (height range for thick disk horizontal luminosity profiles). This value, which we will call f_a, was averaged over all the valid vertical bins. However, because the shape of the vertical thick disk luminosity profile changes in the absence of a thin disk, we calculated a second value, f_b, which measures the same ratio if the thin disk was removed but the thick disk face-on column mass density and the vertical velocity dispersion were kept constant. As seen in Figure 16, $f_b < f_a$.

The f_a and f_b values can be used for estimating the brightness of the thick disk in the range of heights $0 < z < 0.5z_s$, but we have to consider that they have been calculated at low R and

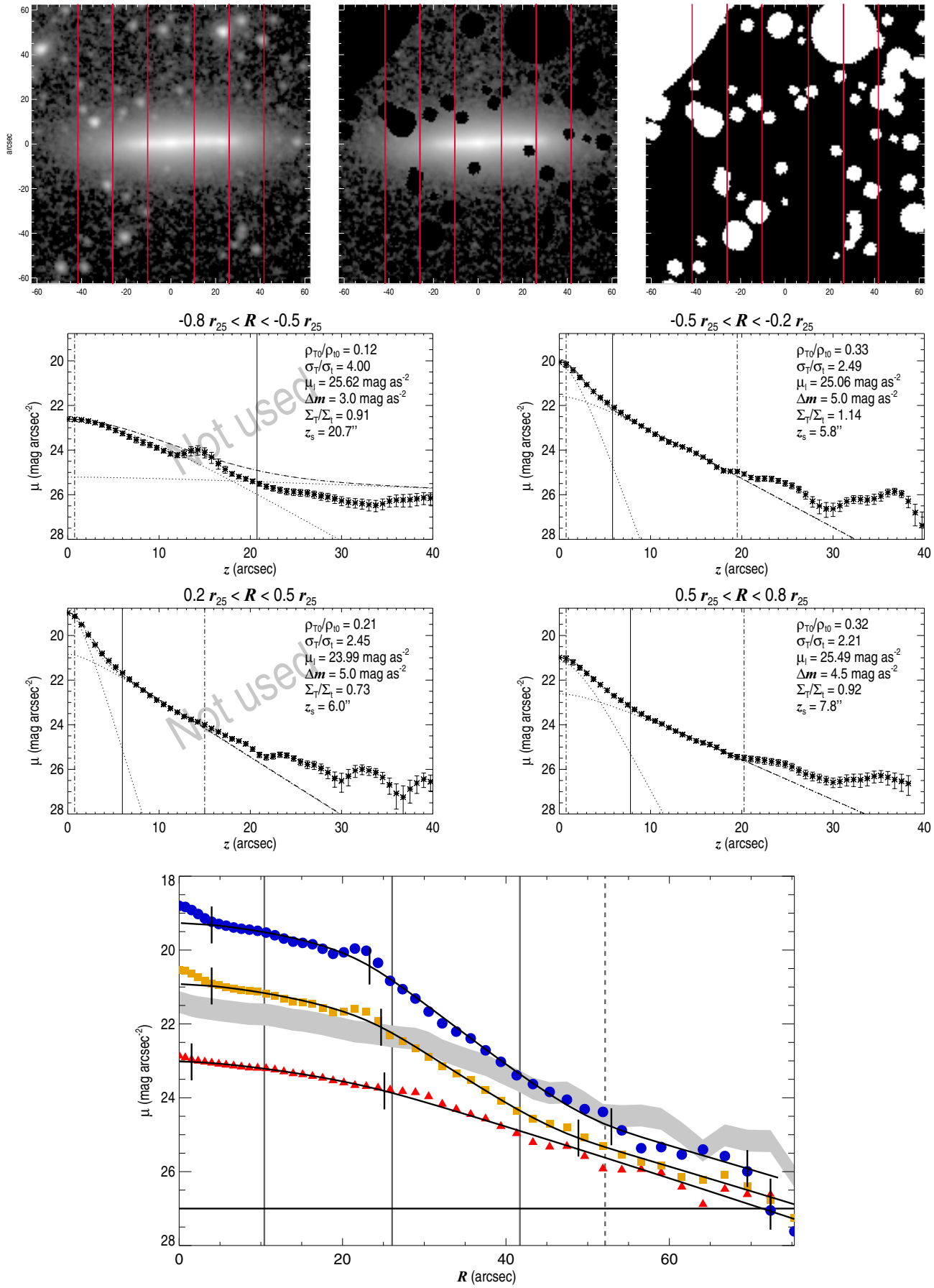

Figure 17. ESO157-049. For a description of how the information is organized in this figure, see the Appendix.
(An extended, color version of this figure is available in the online journal.)

can only be considered a useful approximation to what happens in galaxy outskirts. In Figure 17, the lower limit of the gray area is the estimate of the thick disk brightness at that range ($0 < z < 0.5z_s$) in the absence of a thin disk calculated by moving the red symbols up by a factor f_b. The upper limit of the gray area represents the thick disk surface brightness estimate for the range $0 < z < 0.5z_s$ in the case of a thin disk whose face-on column mass density relative to the thick disk is similar to that found at low R (moving the red symbols up by a factor f_a). Thus, for the outskirts of a galaxy, the lower limit of the gray area symbols represents what we have defined to be the thin disk if it was only the low z part of a thick disk and no significant genuine thin disk was found there.

Of the 26 thin disks with antitruncations, 14 (ESO 157-049, ESO 440-027, IC 1553, NGC 0522, NGC 1163, NGC 1422, NGC 3454, NGC 4330, NGC 4359, NGC 4607, NGC 5529, UGC 06526, UGC 12518, and UGC 12692) are well fitted by the lower limit of the gray area, meaning that they are compatible with the range of projected radii $R > r_a$ being dominated by the thick disk at all heights. In six galaxies (ESO 469-015, IC 1576, UGC 00903, UGC 01970, UGC 07086, and UGC 10288), the thick disk alone does not seem to be bright enough to account for all the light for heights $0 < z < 0.5z_s$ at $R > r_a$. In four galaxies (NGC 1596, NGC 3628, NGC 4081, and UGC 08737), our thick disk brightness estimate at $0 < z < 0.5z_s$ overestimates the actual light emission. For NGC 5084, the antitruncation is an artifact caused by the presence of an extended bulge. Finally, for one galaxy (UGC 10297), the thick disk profile is too dim at $R > r_a$ to be able to obtain any conclusion.

It thus seems that in at least 14 out of 26 antitruncated galaxies, the antitruncation is actually an artifact caused by the presence of a thick disk. This number is probably a low estimate, because of the uncertainties of using f_b for inferring the behavior of the disk in its outskirts.

A legitimate question is that if for $R > r_a$ we are mostly detecting the thick disk at all heights, then why is its horizontal luminosity profile almost always flatter for $z_s < z < z_u$ (red horizontal luminosity profiles) than in the range $0 < z < 0.5z_s$ (blue horizontal luminosity profiles)? This can be explained naturally if we consider that at $R \sim r_a$ there is still a small fraction of stars belonging to the thin disk, meaning that the vertical thick disk luminosity profile becomes more peaked (see Figure 16) than when the thin disk mass fraction becomes negligible for $R \gg r_a$. This progressive broadening of the thick disk vertical luminosity profile with increasing projected radii causes the horizontal luminosity profile for $0 < z < 0.5z_s$ to be steeper than that measured at $z_s < z < 0.5z_u$. Additionally, unmasked faint stars and extended PSF wings are more likely to affect the much dimmer $z_s < z < 0.5z_u$ range, potentially contributing further to making its horizontal luminosity profile shallower.

Here, we have shown that genuine antitruncations are rare (12 at maximum out of 70 or less than ∼15%) and that most of the features which would be considered an antitrucation in a face-on view are actually an artifact caused by the superposition of a thin and a thick disk with different scale lengths. However, it seems that several of the found antitruncations are genuine and could be a signature of a past interaction—as suggested by Laurikainen & Salo (2001). Laurikainen & Salo (2001) showed that many M 51-like interacting galaxies have antitruncations. They used numerical simulations to show that the redistribution of material caused by an interaction may last for several Gyr, which could explain the presence of genuine antitruncations in isolated galaxies. Also, some of the antitruncations which do not seem related to the thick disk could be caused by the presence of outer rings, as suggested by Erwin et al. (2005).

6.3. Galaxies with Circular Velocities Below $v_c = 120\,\mathrm{km\,s^{-1}}$ Have More Massive Thick Disks

In Section 5.1, we found that thick disks with $v_c > 120\,\mathrm{km\,s^{-1}}$ have roughly constant relative masses with respect to the thin disk ($0.2 < M_T/M_t < 0.7$), and that the relative stellar mass of the thick disk increases for $v_c < 120\,\mathrm{km\,s^{-1}}$. This threshold was not noticed in CO11b due to smaller statistics and a larger scatter in data due to less restrictive quality selection criteria. However, it was detected by Yoachim & Dalcanton (2006).

If, as indicated in CO11b, thick disks would have formed in situ at high redshift and have their thin disks formed from gas remaining from the formation process and posterior cold accretion, then at least two factors could contribute to making M_T/M_t larger in less massive galaxies.

1. Supernova feedback is more efficient at removing the gas from shallower potential wells. This is because in a high-mass galaxy, gas expelled by supernovae during the thick disk build-up could eventually come back to the galaxy and be used for building the thin disk. Gas expelled from low-mass galaxies would be less likely to come back.
2. Lower-mass galaxies are dynamically younger than higher-mass ones. All galaxies already formed their thick disk and later started to form the thin disk. Because of the slowest evolution of lower-mass galaxies, their thin disks are younger and less developed, implying a larger fraction of gas in them.

It is important to stress the point that less massive galaxies are likely to expel a larger gas fraction through supernova feedback than massive ones. Indeed, as pointed out by Elmegreen & Elmegreen (2006), if a thick disk formed at high redshift had only ∼20% of the total mass of the disk (as is the case for today's thick disks in some massive galaxies), then its scale height would shrink considerably when the gas which formed the thin disk, the remaining 80% in mass, was accreted. This could cause, if the thick disk scale height was not large enough (several kpc), the thick disks to be indistinguishable from the thin disks in vertical luminosity profiles. The thick disk scale height shrinking would be smaller in a low-mass galaxy accreting a lower fraction of gas (∼50%), which would make the original thick disk formed at high redshift much easier to detect.

Thus, what we observe as thick disks in today's low-mass galaxies would be mostly the original in situ thick disks formed at high redshifts. For massive galaxies, which have expelled less gas through supernova feedback, it is possible that this disk would have shrunk so much that it would be undetectable. In this case, there would be no genuine thick disks, but a continuous distribution of scale heights created by the secular heating of the thin disk by its own overdensities in accordance with the claim from Bovy et al. (2012) for the Milky Way. Significant thin disk heating by satellites is likely to be discarded due to the absence of widespread flares as discussed in CO11b. The thick disk being mostly made of stars stripped from satellites is also discarded because that mechanism would lead thick disks significantly less massive than what is observed (see CO11b for a full discussion on these two points). Radial migration (Schönrich & Binney 2009) could also explain the presence of thick disks in massive galaxies, but fails at explaining the presence of very massive

thick disks in low-mass galaxies which are dynamically younger than high-mass ones.

A way of testing whether M_T/M_t is higher in low-mass galaxies due to a slower dynamical evolution is to recalculate M_t by considering that, in addition to the thin disk stars, it includes the gas disk. If low-mass galaxies were less efficient at forming stars, then the new M_T/M_t would show a flatter trend with the rotation velocity, v_c. To calculate the mass of gas contained in a disk, we used the 21 cm corrected for self-absorption flux from HyperLEDA and we converted it to a gas mass using the expression

$$M_{\rm HI}/M_\odot = 236\, d^2\, f, \quad (7)$$

where f is the area of the 21 cm line profile expressed in mJy km s^{-1} and d is the distance to the galaxy expressed in Mpc (Zwaan et al. 1997). As done in Yoachim & Dalcanton (2006), we made the correction $M_{\rm gas} = 1.4 M_{\rm HI}$ to account for helium and metals, and we did not apply a correction for molecular gas. The new M_T/M_t values have been calculated considering that the absolute 3.6 μm magnitude of the Sun in AB system is $M_\odot = 6.06$ mag (Oh et al. 2008), that $\Upsilon_t = 1$, and that $\Upsilon_T/\Upsilon_t = 1.2$. This has been done for all except three galaxies in the sample. Those three galaxies had no f value available in HyperLEDA. The result of including the gas into the thin disk is shown in Figure 6 in which the diamond symbols represent M_T/M_t once the gas has been included in the thin disk. We note a slight tendency for low-mass galaxies to get their relative thick disk masses lowered by a larger factor by this operation than in the case of high-mass galaxies. When including the gas in the thin disk, the decrease in the thick disk relative mass fraction is $\Delta(M_T/M_t) = -0.27 \pm 0.04$ when $v_c < 120$ km s^{-1} and $\Delta(M_T/M_t) = -0.11 \pm 0.03$ for galaxies with $v_c > 120$ km s^{-1}. This would support the idea of lower-mass disks having a slower evolution than higher-mass galaxies and having transformed less gas into thin disk stars. However, a definitive quantification of this effect cannot be obtained without knowing the mass-to-light ratio of the disks. We are working on this quantification and will publish it in a follow-up paper.

7. SUMMARY AND CONCLUSIONS

Recent works suggest that thick disks are formed in situ at high redshift. So far, the easier way to study thin and thick disks as separate features is by looking at edge-on galaxies.

Breaks (truncations and antitruncations) in disk galaxies have until now mostly been studied for the disk as a whole, without distinguishing the light of the thin and the thick disk. Several theories compete for explaining the origin of such breaks. Truncations have been explained by dynamical arguments related to the conservation of angular momentum during galaxy formation, by star formation thresholds, and by the redistribution of angular momentum by a bar. Antitruncations have in some cases been linked to interactions and mergers.

In order to study a significant sample of edge-on galaxies (70), we produced luminosity profiles of thin and thick disks parallel to galaxy midplanes from the average of the 3.6 and 4.5 μm images from the S^{4}G. The vertical height dominated by each disk was derived from luminosity profiles perpendicular to midplanes done in a similar way to that described in Comerón et al. (2011b). In brief, we fitted the observed vertical luminosity profiles by comparing them with a grid of models made by solving the equations of three gravitationally coupled vertically isothermal disks (thin, thick, and gas disks). We defined the range of heights for which the thick disk dominates that height (named z_s), above which it emits 90% of the light. We defined a height, z_u, at which the 26 mag arcsec^{-2} level was reached for the fitted vertical bins. The thick disk horizontal luminosity profile was made by averaging the light emission for $z_s < z < z_u$ and the thin disk one was made by averaging light in $0 < z < 0.5 z_s$.

Once the thin and thick disk luminosity profiles parallel to midplanes were created, we fitted them with an integrated over the line-of-sight generalization of the function used by Erwin et al. (2008) to describe disks with breaks.

The conclusions of this paper are as follows.

1. The position of our breaks is compatible with those fitted in face-on galaxies.
2. Horizontal luminosity profiles for thin disks are often truncated (77% of cases) and also have a significant number of antitruncations (40% of cases). According to our fits, thick disks truncate with a frequency of 31%, although some extra truncations cannot be discarded at a lower surface brightness than our detection threshold. Antitruncations are rare in our thick disk sample (6%) and are in three out of four cases artifacts caused by an extended bulge.
3. When thick disks truncate, they do so at a radius usually compatible with that of the truncation of the thin disk. However, not all truncated thin disks are associated with a truncated thick disk. This dichotomy suggests two different mechanisms creating truncations: one—necessarily of dynamical origin—affecting both disks and one affecting only the thin disk. Another possibility is that the same mechanism creates a truncation in the thin disk or in both, depending on some galactic property which has not been studied in this paper (such as bar or kinematical properties).
4. Antitruncations in thin disks seem to be related, in more than half of the cases, to the superposition of a thin and a thick disk with different scale lengths. Thus, for those thin disks, the part outside the antitruncation would actually be the thick disk. We estimate the fraction of genuine thin disk antitruncations to be at maximum 15%. This is less than half of those that would be expected from a deep enough fit to a face-on galaxy sample.
5. Because our sample is much larger and better selected than that used in Comerón et al. (2011b), we have been able to further constrain the shape of the relation between the stellar mass of the thick disk relative to that of the thin disk, M_T/M_t, and the galaxy circular velocity, v_c, originally found by Yoachim & Dalcanton (2006) (Figure 6). We found that galaxies with $v_c > 120$ km s^{-1} have a roughly constant M_T/M_t. From $v_c = 120$ km s^{-1} downward, M_T/M_t increases dramatically with, in some cases, $M_T/M_t > 1$. For these galaxies, the high M_T/M_t could be caused by a combination of a high efficiency of supernova feedback that removes gas from the weak potential well of the young galaxy and limits the eventual mass of the thin disk, and a slower dynamical evolution causing the stellar thin disks to be younger and less massive than in higher-mass galaxies. In the latter case, we showed that if we assume the same Υ_T/Υ_t for all galaxies, when gas is included in the mass of the thin disk, galaxies with $v_c < 120$ km s^{-1} have M_T/M_t values that are more similar to those in galaxies with $v_c > 120$ km s^{-1}. This similarity implies that part of the high value for M_T/M_t low-mass galaxies is the result of thin disk youth: the thin disk mass has not formed stars yet.

The authors wish to thank the entire S^{4}G team for their efforts in this project. E.A. and A.B. thank the Centre National d'Études Spatiales for financial support. K.S., J.-C.M.-M., T.K., and T.M. acknowledge support from the National Radio Astronomy Observatory, which is a facility of the National Science Foundation operated under cooperative agreement by Associated Universities, Inc.

We thank our anonymous referee for comments that helped to improve the paper.

This work is based on observations and archival data made with the *Spitzer Space Telescope*, which is operated by the Jet Propulsion Laboratory, California Institute of Technology under a contract with NASA. We are grateful to the dedicated staff at the Spitzer Science Center for their help and support in planning and execution of this Exploration Science program. We also gratefully acknowledge support from NASA JPL/Spitzer grant RSA 1374189 provided for the S^{4}G project.

Funding for SDSS-III has been provided by the Alfred P. Sloan Foundation, the Participating Institutions, the National Science Foundation, and the U.S. Department of Energy Office of Science. The SDSS-III Web site is http://www.sdss3.org/.

SDSS-III is managed by the Astrophysical Research Consortium for the Participating Institutions of the SDSS-III Collaboration including the University of Arizona, the Brazilian Participation Group, Brookhaven National Laboratory, University of Cambridge, Carnegie Mellon University, University of Florida, the French Participation Group, the German Participation Group, Harvard University, the Instituto de Astrofisica de Canarias, the Michigan State/Notre Dame/JINA Participation Group, Johns Hopkins University, Lawrence Berkeley National Laboratory, Max Planck Institute for Astrophysics, New Mexico State University, New York University, Ohio State University, Pennsylvania State University, University of Portsmouth, Princeton University, the Spanish Participation Group, University of Tokyo, University of Utah, Vanderbilt University, University of Virginia, University of Washington, and Yale University.

This research has made use of the NASA/IPAC Extragalactic Database (NED) which is operated by the Jet Propulsion Laboratory, California Institute of Technology, under contract with the National Aeronautics and Space Administration.

APPENDIX

LUMINOSITY PROFILE FITS

The extended Figure 17 includes the vertical and horizontal luminosity profile fits for all the galaxies in our final sample. It also includes the image of each galaxy. The information is organized as follows for each page of the extended figure.

1. The three images in the top row show the average of the 3.6 and 4.5 μm band background-subtracted S^{4}G frames (left), the same image after masking (center), and the used mask (right). The vertical red lines indicate the limits of the fitted vertical bins, the central one being ignored due to the possible presence of a bulge.
2. The next two rows show the fits to the luminosity profiles in these bins. The data points have 2σ statistical error bars, the dashed curve represents the best fit, the dotted curves indicate the contributions of the thin and thin disks. The dash-dotted vertical lines indicate the limits of the range in vertical distance above the mid-plane used for the fit. The vertical solid line indicates z_s for each bin. The profiles in bins which have not been selected for the data processing in this paper (Section 3.4) are indicated with a "Not used" label.
3. The bottom panel shows the horizontal luminosity profiles integrated from $z = 0$ to $z = z_u$ (total; yellow), from $z = 0$ to $z = 0.5z_s$ (thin disk; blue), and from $z = z_s$ to $z = z_u$ (thick disk; red). The black lines indicate fits to those profiles, with vertical intersecting lines indicating the fitting range and the truncation radii. The vertical solid gray lines represent $0.2r_{25}$, $0.5r_{25}$, and $0.8r_{25}$. The vertical dashed line represents r_{25}. The gray area represents the inferred average surface brightness of the thick disk in the range $z = 0$ to $z = 0.5z_s$ in the presence of a thin disk with a relative face-on surface brightness similar to what is found where the vertical luminosity profiles have been successfully fitted (upper limit), and in the absence of it (lower limit), extrapolated from the vertical luminosity profile fits. The bins for which valid vertical luminosity fits have been obtained can be seen in the bottom left of each panel. The errors in the fitted parameters are 2σ fitting errors.

REFERENCES

Abadi, M. G., Navarro, J. F., Steinmetz, M., & Eke, V. R. 2003, ApJ, 597, 21
Aihara, H., Allende-Prieto, C., An, D., et al. 2011, ApJS, 193, 29
Bakos, J., & Trujillo, I. 2012, MNRAS, submitted (arXiv:1207.7023)
Banerjee, A., & Jog, C. J. 2007, ApJ, 622, 335
Barteldrees, A., & Dettmar, R.-J. 1994, A&AS, 103, 475
Bensby, T., Feltzing, S., Lundström, I., & Ilyin, I. 2005, A&A, 433, 185
Bigiel, F., Leroy, A., Brinks, E., et al. 2008, AJ, 136, 2846
Bournaud, F., Elmegreen, B. G., & Martig, M. 2009, ApJ, 707, L1
Bovy, J., Rix, H.-W., & Hogg, D. W. 2012, ApJ, 751, 131
Brook, C., Richard, S., Kawata, D., Martel, H., & Gibson, B. K. 2007, ApJ, 658, 60
Burstein, D. 1979, ApJ, 234, 829
Buta, R. J. 2012, in Planets, Stars, and Stellar Systems, Vol. 6, Series Editor T. D. Oswalt, Volume editor W. C. Keel (New York: Springer) (arXiv:1102.0550)
Buta, R. J., Sheth, K., Regan, M., et al. 2010, ApJS, 190, 147
Clemens, D. P. 1985, ApJ, 295, 422
Comerón, S., Elmegreen, B. G., Knapen, J. H., et al. 2011a, ApJ, 738, L17
Comerón, S., Elmegreen, B. G., Knapen, J. H., et al. 2011b, ApJ, 741, 28, (CO11b)
Comerón, S., Knapen, J. H., Sheth, K., et al. 2011c, ApJ, 729, 18
Dalcanton, J. J., Yoachim, P., & Bernstein, R. A. 2004, AJ, 608, 189
Debattista, V. P., Mayer, L., Carollo, C. M., et al. 2006, ApJ, 645, 209
de Grijs, R., Kregel, M., & Wesson, K. H. 2001, MNRAS, 324, 1074
de Jong, R. S., Seth, A. C., Radburn-Smith, D. J., et al. 2007, ApJ, 667, L49
de Vaucouleurs, G., de Vaucouleurs, A., Corwin, H. G., et al. 1991, Third Reference Catalog of Bright Galaxies (New York: Springer) (RC3)
Elmegreen, B. G., & Elmegreen, D. M. 2006, ApJ, 650, 644
Erwin, P., Beckman, J. E., & Pohlen, M. 2005, ApJ, 626, L81
Erwin, P., Pohlen, M., & Beckman, J. E. 2008, AJ, 135, 20
Fazio, G. G., Hora, J. L., Allen, L. E., et al. 2004, ApJS, 154, 10
Florido, E., Battaner, E., Guijarro, A., Garzón, F., & Castillo-Morales, A. 2006a, A&A, 455, 467
Florido, E., Battaner, E., Guijarro, A., Garzón, F., & Castillo-Morales, A. 2006b, A&A, 455, 475
Florido, E., Battaner, E., Guijarro, A., Garzón, F., & Jiménez-Vicente, J. 2001, A&A, 378, 82
Freeman, K. C. 1970, ApJ, 160, 811
Fuhrmann, K. 1998, A&A, 338, 161
Gilmore, G., & Reid, N. 1983, MNRAS, 202, 1025
Gutiérrez, L., Erwin, P., Aladro, R., & Beckman, J. E. 2011, AJ, 142, 145
Haynes, M. P. 1979, AJ, 84, 1830
Irwin, J. A., Kennedy, H., Parkin, T., & Madden, S. 2007, A&A, 474, 461
Jordi, K., Grebel, E. K., & Ammon, K. 2006, A&A, 460, 339
Kennicutt, R. C., Jr. 1989, ApJ, 344, 685
Kregel, M., & van der Kruit, P. C. 2004, MNRAS, 355, 143
Kregel, M., van der Kruit, P. C., & de Blok, W. J. G. 2004, MNRAS, 352, 768
Kregel, M., van der Kruit, P. C., & de Grijs, R. 2002, MNRAS, 334, 646

Laurikainen, E., & Salo, H. 2001, MNRAS, 324, 685
Lewis, J. R., & Freeman, K. C. 1989, AJ, 97, 139
Loebman, S. R., Roškar, R., Debattista, V. P., et al. 2011, ApJ, 737, 8
Maltby, D. T., Hoyos, C., Gray, M. E., Aragón-Salamanca, A., & Wolf, C. 2012, MNRAS, 420, 2475
Martín-Navarro, I., Bakos, J., Trujillo, I., et al. 2012, MNRAS, accepted (arXiv:1208.2893)
Muñoz-Mateos, J. C., Sheth, K., Gil de Paz, A., et al. 2012, ApJ, submitted
Narayan, C. A., & Jog, C. J. 2002, A&A, 394, 89
Newmark, N. M. 1959, Proc. ASCE, 85, 67
Oh, S.-H., de Blok, W. J. G., Fabian, W., Brinks, E., & Kennicutt, R. C., Jr. 2008, AJ, 136, 2761
Paturel, G., Petit, C., Prugniel, Ph., et al. 2003, A&A, 412, 45
Pérez, I. 2004, A&A, 427, L17
Pohlen, M., Balcells, M., Lütticke, R., & Dettmar, R.-J. 2004a, A&A, 422, 465
Pohlen, M., Beckman, J. E., Hüttmeister, S., et al. 2004b, in Penetrating Bars through Masks of Cosmic Dust, ed. D. L. Block et al. (Cambridge: Cambridge Univ. Press), 713
Pohlen, M., Dettmar, R.-J., & Lütticke, R. 2000, A&A, 357, 1
Pohlen, M., & Trujillo, I. 2006, A&A, 454, 759
Pohlen, M., Zaroubi, S., Peletier, R. F., & Dettmar, R.-J. 2007, MNRAS, 378, 594
Prochaska, J. X., Naumov, S. O., Carney, B. W., McWilliam, A., & Wolfe, A. M. 2000, AJ, 120, 2513
Qu, Y., di Matteo, P., Lehnert, M. D., & van Driel, W. 2011, A&A, 530, 10
Radburn-Smith, D. J., Roškar, R., Debattista, V. P., et al. 2012, ApJ, 753, 138
Schönrich, R., & Binney, J. 2009, MNRAS, 396, 203
Sheth, K., Regan, M., Hinz, J. L., et al. 2010, PASP, 122, 1397
Spitzer, L. 1978, Physical Processes in the Interstellar Medium (New York: Wiley)
Spitler, L. R., Forbes, D. A., & Beasley, M. A. 2008, MNRAS, 389, 1150
Stark, A. A. 1984, ApJ, 281, 624
Trujillo, I., & Pohlen, M. 2005, ApJ, 630, L17
Tsikoudi, V. 1979, ApJ, 234, 842
van Albada, T. S., Bahcall, J. N., Begeman, K., & Sancisi, R. 1985, ApJ, 295, 305
van der Kruit, P. C. 1979, A&AS, 38, 15
van der Kruit, P. C. 1987, A&A, 173, 59
van der Kruit, P. C. 2001, in ASP Conf. Ser. 230, Galaxy Disks and Disk Galaxies, ed. J. G. Funes & E. M. Corsini (San Francisco, CA: ASP), 119
van der Kruit, P. C., & Searle, L. 1981a, A&A, 95, 105
van der Kruit, P. C., & Searle, L. 1981b, A&A, 95, 116
van der Kruit, P. C., & Searle, L. 1982, A&A, 110, 79
Yoachim, P., & Dalcanton, J. J. 2006, AJ, 131, 226
Zwaan, M. A., Briggs, F. H., Sprayberry, D., & Sorar, E. 1997, ApJ, 490, 173